

**Design and Implementation of
Capacitive Micromachined
Ultrasonic Transducers
for
High Intensity
Focused Ultrasound**

by

F. Yalçın Yamaner

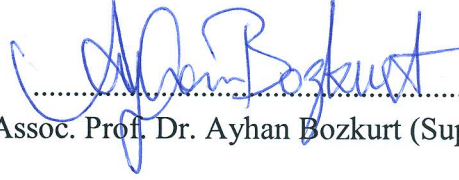
Submitted to the Graduate School of Engineering and Natural Sciences
of Sabanci University in partial fulfillment of
the requirements for the degree of
Doctor of Philosophy

Sabanci University

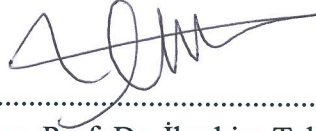
August, 2011

DESIGN AND IMPLEMENTATION OF CAPACITIVE MICROMACHINED
ULTRASONIC TRANSDUCERS FOR HIGH INTENSITY FOCUSED ULTRASOUND

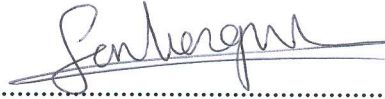
APPROVED BY:



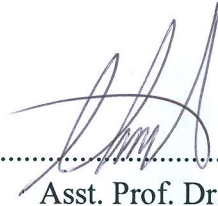
Assoc. Prof. Dr. Ayhan Bozkurt (Supervisor)



Assoc. Prof. Dr. Ibrahim Tekin



Asst. Prof. Dr. Arif Sanlı Ergün



Asst. Prof. Dr. Ahmet Onat



Asst. Prof. Dr. Gözde Ünal

DATE OF APPROVAL: 09.08.2011

© Feysel Yalçın Yamaner 2011
All Rights Reserved

Table of Contents

| | | |
|----------|---|-----------|
| 1 | Introduction | 1 |
| 1.1 | Organization of thesis | 3 |
| 1.2 | Contributions | 4 |
| 2 | High Intensity Focused Ultrasound | 5 |
| 2.1 | HIFU Devices | 6 |
| 3 | The CMUT | 8 |
| 3.1 | Collapse-snap back | 8 |
| 3.2 | Membrane with central mass | 9 |
| 3.3 | Dual-electrode CMUT | 10 |
| 3.4 | Deep Collapse with full-electrode CMUT | 11 |
| 4 | Nonlinear Electrical Circuit Model | 14 |
| 4.1 | The Circuit Model | 15 |
| 4.2 | Membrane Model | 17 |
| 4.3 | Nonlinear Currents, i_c and i_{vel} | 20 |
| 4.4 | Radiation Impedance | 21 |
| 4.5 | Modeling Nonlinear Components in SPICE | 23 |
| 5 | Optimization of CMUT Parameters for HIFU | 28 |
| 5.1 | Operating at half the resonance frequency | 28 |

| | | |
|----------|---|-----------|
| 5.2 | Optimization | 29 |
| 6 | Fabrication | 33 |
| 6.1 | Membrane Side | 34 |
| 6.2 | Substrate Side | 35 |
| 6.3 | Fabricated Devices | 36 |
| 7 | Measurements | 38 |
| 7.1 | Impedance measurements in air | 38 |
| 7.2 | Immersion Experiments | 39 |
| 7.3 | Model Validation | 40 |
| 8 | Conclusion & Future Directions | 44 |
| 9 | Appendix | 46 |
| 9.1 | FEM Model | 46 |

List of Figures

| | | |
|-----|---|----|
| 1.1 | A cross-section view of a CMUT. | 2 |
| 2.1 | A schematic representation of high intensity focused ultrasound lesion production. | 6 |
| 3.1 | A cross-section view of a CMUT. | 9 |
| 3.2 | Non-uniform membrane with a center mass. | 10 |
| 3.3 | A cross-section view of a dual electrode CMUT. | 10 |
| 3.4 | CMUT with full electrode coverage. | 11 |
| 3.5 | Simulated peak-to-peak pressures at the surface of a CMUT when excited by a 40 ns long negative pulses for half electrode and full electrode coverage. The pulse is applied on top of an equal amplitude DC bias and increased step by step. CMUT parameters: $a = 30 \mu\text{m}$, $t_m = 1.4 \mu\text{m}$, $t_g = 0.2 \mu\text{m}$, $t_i = 0.4 \mu\text{m}$ | 12 |
| 3.6 | Transmit sensitivity of CMUT operated in deep collapse mode. Excited by a 40 ns long, 5-V pulse while the bias is being monotonically increased (circles) and monotonically decreased (diamonds). The sudden jump in the figure is a result of transition stage between collapsed and uncollapsed states. CMUT parameters: $a = 30 \mu\text{m}$, $t_m = 1.4 \mu\text{m}$, $t_g = 0.2 \mu\text{m}$, $t_i = 0.4 \mu\text{m}$ | 13 |

| | | |
|------|---|----|
| 4.1 | Representative cross section of a circular membrane with radius a , thickness t_m and gap height of t_g . Top electrode is the conductive silicon wafer. t_i is the insulating layer thickness above the gap. The bottom electrode is a metal layer. | 16 |
| 4.2 | Nonlinear equivalent circuit model of a CMUT. | 16 |
| 4.3 | The resonant frequency of the membrane as determined from L_{rms} and C'_{rms} for various t_m/a values. C'_{rms} is the corrected capacitor value to accurately model resonant frequency (left). Membrane impedance is plotted for a radius of 280 μm and a membrane thickness of 92 μm (right). | 19 |
| 4.4 | The configuration of CMUT array for different number of cells. | 21 |
| 4.5 | RLC model for the normalized radiation resistance and reactance of a single CMUT cell (left) and an array of CMUT (right). | 21 |
| 4.6 | The normalized radiation impedance of a single CMUT (top) and a CMUT array of 7 cells (left) and 19 cells (right) with the RLC model and actual values. | 23 |
| 4.7 | SPICE Model. The radiation impedance is modeled by R, L, C circuit components. N represents the number of cells in the array. | 24 |
| 4.8 | The static deflection of membrane center as calculated by FEM and the circuit model ($a = 30 \mu\text{m}$, $t_m=2 \mu\text{m}$, $t_i=0.1 \mu\text{m}$, $t_g=0.1 \mu\text{m}$ (A). $a = 300 \mu\text{m}$, $t_m=100 \mu\text{m}$, $t_i=0.4 \mu\text{m}$, $t_g=0.1 \mu\text{m}$ (B).) | 25 |
| 4.9 | Single CMUT cell in vacuum. 1 cycle 20V AC voltage at 7.3 MHz with 20V DC voltage (left) and 4 cycle 100Vpeak cosine burst at 1 MHz (right) is applied. | 26 |
| 4.10 | 2 cycle 100Vpeak cosine burst at 1.3 MHz is applied to a single CMUT under fluid loading ($a=300 \mu\text{m}$, $t_m=100 \mu\text{m}$, $t_g=100 \text{ nm}$, $t_i=400 \text{ nm}$.) | 27 |

| | | |
|------|--|----|
| 4.11 | Observed surface pressure. 2 cycle 100V _{peak} cosine burst at 1.44 MHz is applied to CMUT element with 7 cells under fluid loading ($a=280 \mu\text{m}$, $t_m=92 \mu\text{m}$, $t_g=110 \text{ nm}$, $t_i=350 \text{ nm}$.) | 27 |
| 5.1 | The center displacement of the membrane for different t_g under a continuous 100V 1.5MHz sinusoidal signal ($a=289.5 \mu\text{m}$, $t_m=130 \mu\text{m}$, $t_i=100 \text{ nm}$). | 30 |
| 5.2 | The flowchart of the optimization. | 32 |
| 6.1 | (a)3 inch Conductive silicon wafer with a thickness of $100 \mu\text{m}$. (b) Thermal oxidation (c) Lithography and oxide etching to form the cavities | 34 |
| 6.2 | The photograph of the completed process on membrane side. | 35 |
| 6.3 | (a)Borosilicate glass wafer (b)Lithography and glass etching for bottom electrode (c)Ti/Au deposition (d)Cleaning | 36 |
| 6.4 | The photograph of the completed process on glass side. | 36 |
| 6.5 | After anodic bonding, lead wires are connected using conductive epoxy. | 37 |
| 6.6 | Fabricated CMUTs. | 37 |
| 7.1 | Picture of the experimental setup. | 41 |
| 7.2 | Schematic of the experimental setup with the devices. | 41 |
| 7.3 | Measured surface pressures for different peak voltages at 1.44 MHz. | 42 |
| 7.4 | Normalized frequency spectrum of the surface pressure for different peak voltages. | 42 |
| 7.5 | The SPICE model with the fabricated device parameters. | 43 |

| | | |
|-----|--|----|
| 7.6 | 5 cycle 125V _{peak} cosine burst at 1.44 MHz is applied to the CMUT element. After the measurement is corrected for diffraction, and attenuation losses; the result is multiplied by $Z_r(w)/R_r(w)$ in frequency domain and its inverse fourier transform is compared to the pressure obtained from SPICE model. | 43 |
| 9.1 | Representative finite element model of the transducer created in ANSYS. Membrane is modeled with PLANE82 elements. TRANS126 elements are generated using EMTGEN command. | 46 |
| 9.2 | Comparison of the deflection profile of a CMUT in collapse state simulated using for TRANS126 and CONTA172/TARGE169 contact elements. CMUT parameters: $a = 30 \mu\text{m}$, $t_m = 1.4 \mu\text{m}$, $t_g = 200 \text{ nm}$, $t_i = 0.4 \mu\text{m}$ | 48 |
| 9.3 | Representative finite element model including the fluid medium which is extended using FLUID129 absorbing elements. | 49 |
| 9.4 | The FEM model of a CMUT element with infinite cells. | 50 |
| 9.5 | 3D FEM model of a CMUT element with 7 cells. A quarter model of the array and the fluid medium is used for the simulations. | 50 |
| 9.6 | Expanded view of the 3D quarter model of a CMUT element with 7 cells. | 51 |

List of Tables

| | | |
|-----|---|----|
| 4.1 | Membrane material properties used in simulations. | 18 |
| 4.2 | Component values for the radiation impedance model with different number of cells in the array where $R_n = \pi a^2 \rho_0 c / N$ | 22 |
| 5.1 | Design Comparisons at 3 MHz. ($t_i=200$ nm, $N=7$, 100 V _p ,) | 31 |
| 6.1 | Properties of the fabricated devices. | 37 |
| 7.1 | Resonant frequencies in air. | 39 |
| 7.2 | The parameters of the tested CMUTs on glass wafer. | 39 |

Acknowledgement

I would like to express my gratitude to all those who gave me the opportunity to complete this thesis.

First of all, I thank to my supervisor, Dr. Ayhan Bozkurt. I have always felt fortunate for being a student under his supervision. And I am having the honor of being his first doctorate graduate.

I would like to thank Dr. Levent Degertekin for inviting me to the Georgia Institute of Technology. The research experience that I have gained in his group, provided me the enthusiasm to create this thesis.

I would like to acknowledge the financial support of TUBITAK, the project grants provided the necessary of the financial support for this research.

The great collaboration between Sabanci and Bilkent University made this dissertation possible. I am so grateful to meet Prof. Abdullah Atalar and Prof. Hayrettin Koymen and get benefit from their wide experiences and knowledge. They have always welcomed me in Bilkent University and provided the guidance to finish this research. I specially thank my colleague, Selim Olcum, for his support, share and help. He always made me feel at home when I was in Bilkent University.

I would like to thank the members of my thesis committee, Dr. Sanli Ergun, Dr. Ibrahim Tekin, Dr. Gozde Unal, and Dr. Ahmet Onat for their detailed review, constructive comments and advices.

Thank also to my family for supporting and encouraging me in my studies.

Last but not least, I would like to thank my wife, Melis, for being my inspiration and motivation.

Yalçın Yamaner

ABSTRACT

DESIGN AND IMPLEMENTATION OF CAPACITIVE MICROMACHINED ULTRASONIC TRANSDUCERS FOR HIGH INTENSITY FOCUSED ULTRASOUND

F. Yalçın Yamaner

Ph.D. in Department of Electrical and Electronics Engineering

Supervisor: Assoc. Prof. Dr. Ayhan Bozkurt

High intensity focused ultrasound (HIFU) is a medical procedure for noninvasive treatment of cancers. High intensity focused ultrasound is used to heat and destroy the diseased tissue. Piezoelectricity has been the core mechanism for generation of ultrasound waves in the treatment. Focusing can be done by using spherically curved transducers or using a lens or electronically steering sound waves by using phased arrays. Current research in HIFU technology targets the development of MR-guided miniaturized ultrasonic probes for treatment of cancerous tumors. Capacitive micromachined ultrasonic transducer (CMUT) is an alternative technology to generate and detect ultrasound. CMUT consists of a suspended membrane. The advances in CMUT technology, enables fabricating tiny transducer arrays with wide bandwidth makes them a strong candidate for the application. In this thesis, a new methodology is proposed to design and operate CMUTs to generate high pressures under continuous wave excitation. An accurate nonlinear circuit model of CMUT is developed and the model is carried into a SPICE (Simulation Program with Integrated Circuit Emphasis) simulator for fast simulations. The model includes the radiation impedance of the array, thus the operation in a fluid environment can be simulated. The model is verified by doing FEM simulations. The circuit model provides a novel optimization tool for CMUT operating in non-collapse mode. The optimized CMUT parameters are presented and a sample fabrication is done using anodic bonding process. With the process, a 100 μm thick silicon wafer is bonded to a glass substrate. A new driving scheme is proposed without a need of DC voltage. Thus, the charge

trapping problem in CMUT operation is eliminated. The fabricated device provides 1.8 MPa surface pressure with -28dB second harmonic for a maximum 125V drive voltage at 1.44 MHz which is currently a state of art performance of a CMUT under continuous wave excitation.

Keywords : Capacitive Micromachined Ultrasonic Transducer, CMUT, High Intensity Focused Ultrasound HIFU, Large Signal Circuit Model, Microfabrication, Anodic Bonding

ÖZET

YOĞUNLUKLU ODAKLANMIŞ YÜKSEK FREKANSLI SES TEDAVİSİ İÇİN KAPASİTİF MİKROİŞLENMİŞ ULTRASONİK DÖNÜŞTÜRÜCÜLERİN TASARIMI VE GERÇEKLEŞTİRİLMESİ

F. Yalçın Yamaner

Elektrik Elektronik Mühensiliği Bölümü, Doktora

Tez Danışmanı: Doç. Dr. Ayhan Bozkurt

Kanser tedavisinde çığır açan yöntemlerinden biri olan yoğunluklu odaklanmış yüksek frekanslı ses tedavisi (HIFU) gelişen teknolojiyle birlikte popüler bir hal almaktadır. Prensip olarak lokalize tümörün ısıtılarak tahrip edilmesini mümkün kılar. Vücut içerisinde bir noktaya odaklanmış yüksek frekanslı ses dalgaları, akustik enerjinin ısı enerjisine dönüşümüyle o noktadaki sıcaklığın artmasına neden olur. Belirli sıcaklığın üzerine çıktığında hücre ölümü başlar. Odak noktadaki kanserli hücrenin ölümüyle tedavi tamamlanır. Oldukça hedefe yönelik bir tahrip olması ve bilindik yan etkilerinin olmaması tedavinin popülerlik kazanmasındaki önemli etkenlerdir. Ses kaynağı olarak pizeoelektrik teknolojisi kullanılmakta ve bütün sistem bu teknolojinin üzerine inşa edilmektedir. Yarı iletken teknolojisinin ilerlemesi daha küçük yapıda sistemlerin oluşmasına imkan tanıyarak damar içinde de tedavinin kullanılmasına olanak sağlamaktadır. Bu amaçla sistem minyatürizasyonu hedeflenmektedir. Kapasitif mikroışlenmiş ultrasonik dönüştürücüler (CMUT) piezoelektrik dönüştürücülere göre yeni bir teknolojidir. Mikro-elektromekanik (MEMS) teknolojisi ile üretilen bu dönüştürücüler, piezoelektriklere göre yarı iletken teknolojisine daha uyumludur. Bunun yanında hareket eden zar yapısı sayesinde daha geniş bantlıdır. Uzun yıllar süren araştırmalar neticesinde CMUT üretimi bir yarıiletken üretim teknolojisiyle rahatlıkla üretilmekte ve elektronik entegrasyonu yapılabilir. Yapılan çalışmalarda bu teknolojinin sağladığı faydalar ortaya konmuş ve yakın gelecekte ticarileşmesi beklenmektedir. Bu tezde, HIFU için bir CMUT tasarımı yapılmış ve gerçekleştirilmiştir. Uygulamaya yönelik bu tasarım için bir

optimizasyon metodu geliştirilmiş ve okuyucu bilgisine sunulmuştur. Optimizasyon öncesinde CMUT için lineer olmayan etkileri de içerecek şekilde bir devre modeli oluşturulmuştur. Bu devre modeli CMUT konvansiyonel çalışma modu için oluşturulmuştur. Bu modun tercih edilmesindeki en önemli etken uygulama sırasında oluşacak harmoniklerin minimuma indirilmesini sağlayarak ısı kaybının optimize edilmesidir. Çökme ve derin çökme modlarının lineer olmayan etkileri arttırması, çıkıştaki ikincil harmonik seviyesini de arttırarak akustik enerjinin dönüştürücü yüzeyinde ısı olarak kaybına sebebiyet vermektedir. Aynı şekilde bu modlarda zar yapının sürekli bir şekilde alt tabana yapışıp ayrılması sonucu oluşabilecek beklenmedik zaman farklılaşmaları da harmonik seviyesini arttırmaktadır. Çökme modunun olmadığı bölge HIFU operasyonu için oldukça uygundur. Devre modeli, sonlu eleman model analizleri (FEM) ile sınanmış, ve doğruluğu arttırılmıştır.

Ortamın etkileri gözetlendiğinde dönüştürücünün gördüğü radyasyon empedansının performans üzerindeki etkisi büyüktür. Radyasyon empedansı CMUT dizisinin yapısına; her bir hücrenin dizi içerisindeki konumuna, aralarındaki mesafelere, karşılıklı etkileşimlerine ve en önemlisi frekansa göre farklılıklar göstermektedir. Radyasyon empedansı modellenerek devre modeli içerisine yerleştirilmiş ve gerçek çalışma koşullarının modellenmesi sağlanmıştır. Operasyon esnasında maksimum zar hareketi sağlanarak çıkış gücünün arttırılması hedeflenmiştir. Bu amaçla CMUT radyasyon direncinin maksimum olduğu noktada operasyon sağlanarak çalışılan ortama maksimum güç transferi sağlanmıştır.

HIFU operasyonunda dönüştürücülere elektriksel olarak yüksek genlikli ve sürekli sinüsoidal dalgalar uygulanmaktadır. Geleneksel olarak CMUT bir DC gerilimin üzerine eklenmiş bir AC gerilimle çalışmaktadır. DC gerilim zar yapının belirli bir seviye bükülmesini ve gerilmesini sağlayarak hareketin uygulanan AC gerilimin frekansı ile aynı olmasını sağlamaktadır. Fakat uygulanan DC gerilim elektrotlar arasındaki yalıtkan bölgede yük birikimine sebep olarak CMUT performansını düşürmektedir. Bu etkinin ortadan kaldırılması amacıyla DC kullanılmayarak CMUT lar sadece çalışma frekansının yarısında uygulanacak AC sinyal ortaya konmuş ve deysel olarak gösterilmiştir. Yükleme problemi (charging prob-

lem) olmadan alıřtırılan dnüştürücüler uzun süre uygulanan elektriksel sinyale performans düşüşü olmadan tutarlı cevap verebilmektedir.

Üretilen dnüştürücüler 2.88 MHz'de, 125V sinyal genlięi altında, 1.8 MPa yüzey basıncını -28dB ikincil harmonik seviyesiyle üretebilmektedir. Uygulanan sinyalin frekansı 1.44 MHz'dir. Elde edilen basın ve ikincil harmonik seviyesi uygulanan bu elektriksel sürekli dalga altında řu ana kadar elde edilmiş en yüksek seviyedir.

Optimizasyon sonrası elde edilen dnüştürücü yapısı, kalın bir zar tabakasının oluşturulmasını gerektirmektedir. Bu amaçla zar malzemesi olarak inceltilmiş silikon taban seçilmiş ve anodik yapıştırma metodu kullanılarak silikon taban cam tabana yapıştırılmıştır.

Anahtar Kelimeler : Kapasitif Mikroışlenmiş Ultrasonik Dnüştürücüler, CMUT, Yoęunluklu Odaklanmış Yüksek Frekanslı Ses Tedavisi, HIFU, Medikal Ultrason, Eşdeęer Devre Modeli, Mikrofabrikasyon, Anodik Yapıştırma

Chapter 1

Introduction

High intensity focused ultrasound (HIFU) has become increasingly popular for non invasive and minimally invasive cancer therapy. In addition to being as effective as its existing alternatives, such as radiotherapy, HIFU treatment of tumors is significantly safer. Current research in HIFU technology targets the development of MR-guided miniaturized ultrasonic probes for treatment of cancerous tumors. Capacitive micromachined ultrasonic transducer (CMUT) is an alternative technology to generate and detect ultrasound [1–3]. Fig. 1.1 shows a cross section view of a conventional CMUT structure. The technology of CMUT has made a high progress since it was first introduced. Recent designs, operating and fabrication methods are all promising and make CMUT a strong candidate for ultrasonic applications [4–9]. Using silicon micromachining, CMUTs can be fabricated with different geometries and operating frequencies on a single wafer with an accuracy of nanometers which is difficult for piezoelectrics [10]. Smaller transducer elements can be fabricated on chip, so the overall device size can be reduced. Conductive silicon can be used as metal layers of CMUTs, removing the need of metal, so that electromigration effects can be eliminated which occur due to high currents in high power continuous wave (CW) operation. Silicon is also a thermally conductive material and its usage increases the heat dissipation in the device which is an important problem with PZT transducers [11, 12]. In other words, self heating of the transducer will be much less

than PZT transducers. By the use of CMUTs, skin burns can be eliminated in the region where the transducer is in contact with the body. Furthermore, silicon and silicon dioxide are MRI compatible materials [13]. So CMUTs can easily be used within MRI. Recent designs have been presented for non-invasive cancer therapy of lower abdominal cancers using CMUTs [14].

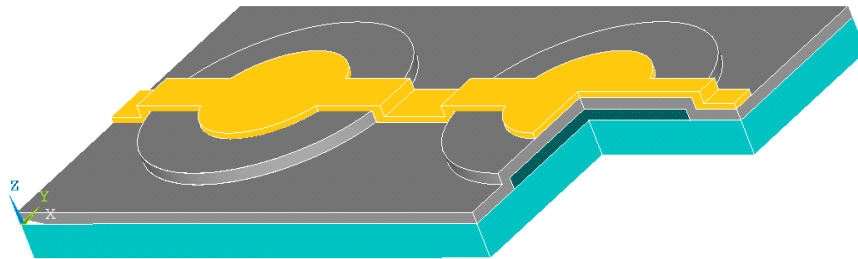


Figure 1.1: A cross-section view of a CMUT.

Recently, it has been demonstrated that CMUTs can be used as HIFU transducers [15], however the pressure level and the second harmonic at the output need to be reconsidered and an optimization is required on CMUT parameters to increase the delivered sound energy.

The joint efforts of CMUT research groups at Bilkent University and Sabanci University to solve the pressure level issue, resulted in a new operation method that has been named as the “deep collapse mode”. This highly non-linear operation mode enables the generation of significantly larger output powers [16]. However, collapse mode may not be suitable for continuous wave of operation due to CMUTs relatively high amplitude harmonic content that is a natural result of the non-linearity of the device.

In this thesis, a new methodology is proposed to design and operate CMUTs to generate high pressures and low harmonics. For a selected frequency of operation, CMUT geometry can be optimized to get high power. The optimization requires a fast simulation tool. Finite element based CMUT simulation tools take too much time for an optimization, especially when the array size is large and the operation is in fluid. Thus, the nonlinear electrical circuit model in [17] which simulates the CMUT

behavior is used for the optimization. First, the circuit is improved by including a realistic radiation impedance model of CMUT array, then the accuracy of the circuit is increased by further modification on circuit parameters by doing finite element simulations. The improved circuit model can be used as a fast simulation tool for the uncollapsed operation mode. It includes the radiation impedance of the array, thus the operation in a fluid environment can be simulated. The circuit can be simply performed using a freely available SPICE circuit simulator. The modeled circuit gives the output pressure for any given CMUT dimensions and input voltage. A transient simulation of a fluid loaded array can be done in seconds by the proposed circuit model. The optimization in this work was done in a SPICE environment using the proposed model. The accuracy of the circuit is tested in comparison with the FEM model. CMUTs were fabricated with high membrane thickness and low gap heights using anodic bonding technology. The important charge trapping issue in CMUT operation has been eliminated by driving CMUTs at half the operating frequency without a DC voltage. It has been shown that a DC voltage bias is not necessary for transmit operation to obtain high output pressure levels.

1.1 Organization of thesis

Chapter 1 provides a brief introduction of the thesis. The targeted application, HIFU, is overviewed and the compatibility and advantages of CMUT technology are discussed. The contributions of the author are given. In Chapter 2, HIFU operation is described in detail and the current devices and literature search on the topic are given. In Chapter 3 introduces CMUT and its structure. The different operating methods to improve the transducer efficiency are shown. The recently discovered operation mode, “deep collapse mode”, is briefly described and the improvement in the transmit pressure is shown. Chapter 4 constructs the base of this thesis. A novel nonlinear circuit model to simulate CMUT behavior is introduced. The creation of the model using a SPICE tool, is explained. The model enables the optimization of CMUT parameters. The components in the model are examined in separate sections.

And the overall model performance is compared and tuned with FEM. In Chapter 5, a methodology for optimizing CMUT parameters to get high power is proposed. The methodology is developed over the model which is described in the previous chapter. An example of an optimum design is given. Chapter 6 describes a new fabrication method of CMUTs. First fabricated CMUTs with thick membranes are introduced. Anodic bonding is used to fabricate CMUTs. Prior to bonding the two wafers are separately processed, thus the fabrication is divided into two sections. The fabrication steps are shown. In Chapter 7, the experiments on the fabricated CMUTs are presented. The experimental setup for the CW operation is shown. Lastly, the accuracy of the SPICE model is once more verified with the experimental result in this chapter. Chapter 8 concludes the thesis.

1.2 Contributions

This thesis covers a part of the collaborated research of CMUT research groups at Bilkent University and Sabanci University. The proposed idea of CMUT optimization for high power is realized in this thesis. The developed nonlinear circuit model of CMUT, by the group at Bilkent University, is improved in terms of accuracy and the model is carried into a SPICE simulator for fast simulations. The created radiation impedance model for the circuit, provided a novel optimization tool for CMUT. The FEM simulations done in this thesis, provide verification of the circuit performance. An optimization methodology is proposed and applied over the improved circuit model. The Bilkent University's clean room facilities enabled the environment to fabricate a sample device. The device provides 1.8 MPa surface pressure with -28 dB second harmonic with a maximum 125V drive voltage which is currently a state of art performance of a CMUT under a continuous wave. A new driving scheme is proposed without a need of DC voltage. Thus, the charging problem is eliminated. Measurements also provided further verification of the proposed circuit. With the optimized parameters, it has been shown that pressure levels up to 4.3 MPa can be easily achieved.

Chapter 2

High Intensity Focused Ultrasound

High intensity focused ultrasound (HIFU) is a state of the art cancer treatment technique. Treatment is done by destruction of the abnormal tissue using high energy focused sound waves (Fig. 2.1). Acoustic absorption converts acoustic energy into thermal energy. Acoustic absorption is proportional to the acoustic intensity as well as acoustic absorption coefficient (attenuation coefficient). Thus, focused ultrasound is able to confine the thermal energy generation to a predetermined controllable focal spot. When the temperature reaches a certain level, the intervening tissue is thermally coagulated. Unlike radiotherapy or laser light treatment, HIFU does not use ionizing radiation. Thus, it works without harming the surrounding healthy tissues. The method even has no known side effects. Treatment is more effective when the abnormal tissue is concentrated into a small volume. By scanning the focal point, a volume can be treated without the need for a traditional operation. The interest in HIFU treatments of breast, brain, liver, bone, kidneys, prostate and uterine fibroids is increasing and the progress is promising [18].

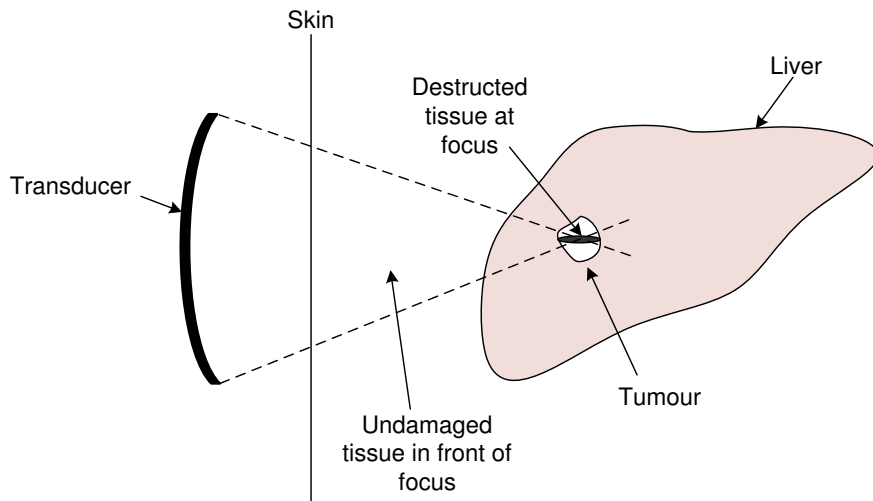


Figure 2.1: A schematic representation of high intensity focused ultrasound lesion production.

2.1 HIFU Devices

In the 1950s, cross-cut planar quartz crystals with converging lenses were used for HIFU [19]. Later on, the introduction of piezoelectric ceramic transducers changed the principle of the operation. Using these materials, both single element unfocused [20] and mechanically focused [21] transducers have been developed and optimized for different ultrasonic operations. Dynamic electronic focusing have also been investigated for the therapy [22]. Extracorporeal devices mainly target organs. They require high focal length, high intensity; thus, they operate at relatively lower frequencies (1.0 - 1.7 MHz). Transrectal devices target prostate. They operate at frequencies between 2.25 MHz and 4 MHz and are smaller in size as compared to extracorporeal ones [23].

There are many piezoelectric transducer based extracorporeal HIFU devices implemented by research groups and companies. One such device has been designed by Haar, et. al. for extracorporeal use [24]. A spherical lead zirconate titanate (PZT) ceramic transducer of 10 cm diameter and 15 cm focal length is used. The transducer operates at 1.7 MHz. Another device has been built in Chongqing HAIFU Technology Company, China. It includes a 12 cm diameter PZT transducer

which has a focal length of 10-16 cm, and operates at either 0.8 MHz or 1.6 MHz. It also has a built in 3.5 MHz diagnostic scanner [25]. Yet another extracorporeal device designed by GE Medical Systems uses magnetic resonance (MR) compatible 10 cm diameter transducer. Transducer operates at 1.5 MHz and has a focal length of 8 cm [26]. Other extracorporeal device designs can be found in the literature [27].

An example for a transrectal device is the probe that has been developed by Sonablate Focus Surgery Inc., USA. The probe contains elements that both image and treat prostate through the intact rectal wall. 4 MHz PZT transducers are used and the focal length of the device can be set to 3.0 cm, 3.5 cm or 4.0 cm. Depending on the focal length the intensity at the focus changes between 1680 - 2000 W cm⁻² [28]. Another probe by a therapeutic ultrasound company, called EDAP TMS, uses a rectangular transducer of focal length 4 cm with an operating frequency of 2.25 - 3.0 MHz. The intensity of the transducer at the focus is 1000 W cm⁻². The probe has a built-in 7.5 MHz imaging element [29].

The devices are dominated by piezoelectricity. The improvement in the performance of CMUT, makes them a strong candidate in the field. The flexibility in the fabrication, enables to design and fabricate a CMUT operating at a specific frequency required for the application. Recently, Wong et al. demonstrated a HIFU device with CMUTs operating at 2.5 MHz. The obtained peak-to-peak pressure level is around 1.4 MPa (16.3 W/cm²) with 80V DC voltage and 130V_{pp} AC voltage [14]. A focal intensity of 85 W/cm² is measured.

Chapter 3

The CMUT

The Capacitive Micromachined Ultrasonic Transducer (CMUT) consists of a thin membrane that vibrates with electrostatic actuation (Fig. 3.1). The voltage applied between the two electrodes of a CMUT provides the electrical force that is required to move the membrane. The main advantage of this technology is the low mechanical impedance of the thin membrane which eliminates the need for matching layers as compared to piezoelectric transducers. Although the idea of an electrostatic transducer is as old as piezoelectricity, the electric field requirements, on the order of million volts per centimeter, made them unrealizable for decades [3]. Advances in the microfabrication technologies allowed the fabrication of tiny gaps, in the order of sub-microns, between the electrodes, enabling GV/m electric fields [10]. While providing numerous advantages over the piezo technology, power output (which is referred to as “transmit sensitivity”) has always been a shortcoming of the device. Various solutions have been offered to alleviate this problem.

3.1 Collapse-snap back

To increase the transmit pressure, Bayram et al. introduced the collapse-snapback mode [29]. In this mode of operation, the CMUT membrane is brought in and out

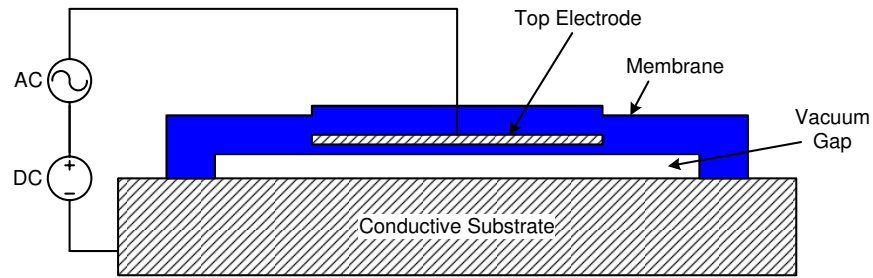


Figure 3.1: A cross-section view of a CMUT.

of contact with the substrate of every transmission cycle to maximize the volumetric displacement [30]. The usage of this unstable region increases the output pressure. The voltage required to collapse the membrane differs from the voltage required to snapback the membrane. After membrane collapses the voltage is reduced until the membrane snapbacks. Although this method successfully increases the maximum transmit pressure around 5 dB [4, 5], it can be problematic due to the nature of the snap-back motion which causes an uncontrolled timing of output signal.

3.2 Membrane with central mass

Another design specification that has been shown to improve the device performance is the membrane shape of the CMUT, which has been investigated by several groups. One method is placing a center mass on the membrane to operate CMUT more in a piston shape as shown in Fig. 3.2 [31, 32], which results in 2 dB improvement in the transmit sensitivity. The resonant frequency of the CMUT has to be carefully considered in that case. Otherwise, undesired vibration modes starts to dominate in the operating region. Mass material could be gold or the membrane itself could be shaped by leaving a mass at the center.

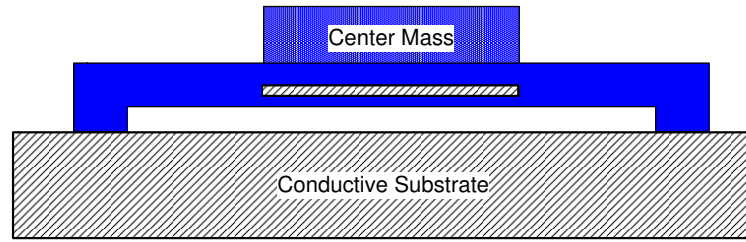


Figure 3.2: Non-uniform membrane with a center mass.

3.3 Dual-electrode CMUT

The dual-electrode CMUT structure has two smaller electrodes placed close to the supports in addition to the center electrode (Fig. 3.3). These side electrodes can be used to move the center of the membrane the entire gap distance without collapse. This effect is known as “leveraged bending” [33].

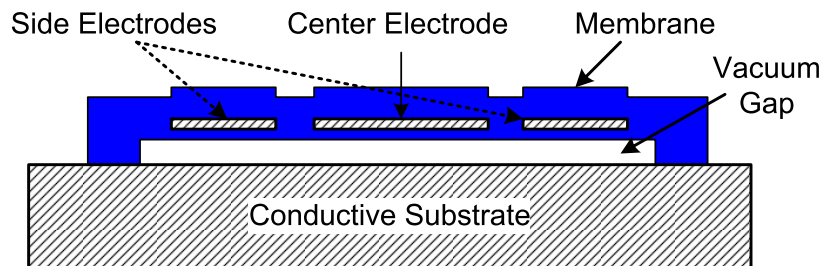


Figure 3.3: A cross-section view of a dual electrode CMUT.

This structure provides a superior receive sensitivity. In receive mode, the membrane shape can be adjusted by the side electrodes so that center receive electrode is brought closer to the bottom electrode which results in higher receive sensitivity [34]. On the other hand, using side electrode actuation increases the CMUT membrane motion from $1/3$ of the gap to almost full gap without collapsing the membrane, which results in increased transmit pressure. However, as the side electrodes are close to the membrane posts, the required voltages levels to bend the membrane are high as compared to the conventional CMUTs with center electrode [35].

3.4 Deep Collapse with full-electrode CMUT

We have recently demonstrated that the region beyond the collapse is a powerful region to operate CMUTs. The “beyond the collapse”, here, means that rather returning back the membrane to its initial uncollapsed position, membrane can be operated further in the collapsed state. The discovery of this mode is done in the tests of fabricated different electrode sized CMUTs. In order to describe this operation, the importance of electrode coverage needs to be underlined.

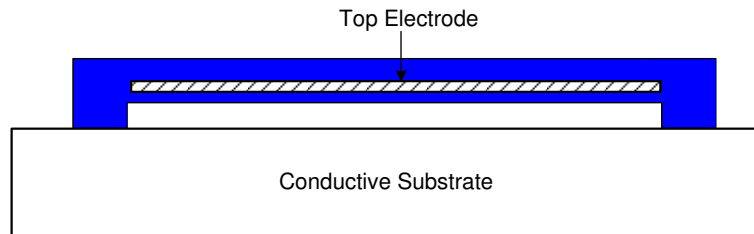


Figure 3.4: CMUT with full electrode coverage.

The electrode coverage of a CMUT plays a major role in both transmit and receive operations. Usually, CMUTs are designed with half electrode coverage for the receive mode in order to optimize the receive sensitivity [36]. However, this may not be optimum for the transmit operation. The maximum collapsed area of the membrane is limited by the electrode sizes. When a full electrode structure is used, the collapsed area can be increased by increasing the applied voltage. Since the contact radius is increased, the membrane stores more energy and delivers more acoustic energy into the medium when it releases. Staying in the collapse mode and using the energy beyond the collapse provides more than 40 kPa/V transmit sensitivity (Fig. 3.6). The larger electrode coverage enhances the electrical field, thus the total force increases over the entire plate and the required voltage to collapse the membrane is also reduced.

The Fig. 3.5 shows the benefit of full electrode coverage as compared to half electrode coverage. As seen from the figure pressure amplitude saturates after a certain increase in the bias voltage. The maximum collapsed region of the membrane is limited by the electrode region. Thus, further applied voltages do not enhance the

membrane movement. On the other hand, full electrode CMUT still gets benefit from the applied voltage and forces the whole membrane area to collapse and increases the mechanical energy stored in the membrane. The Fig. 3.4 shows a cross-section view of the full electrode CMUT where the electrodes cover the whole membrane area. We predicted that more than 6 MPa peak-to-peak pressure can be observed by using this mode of operation.

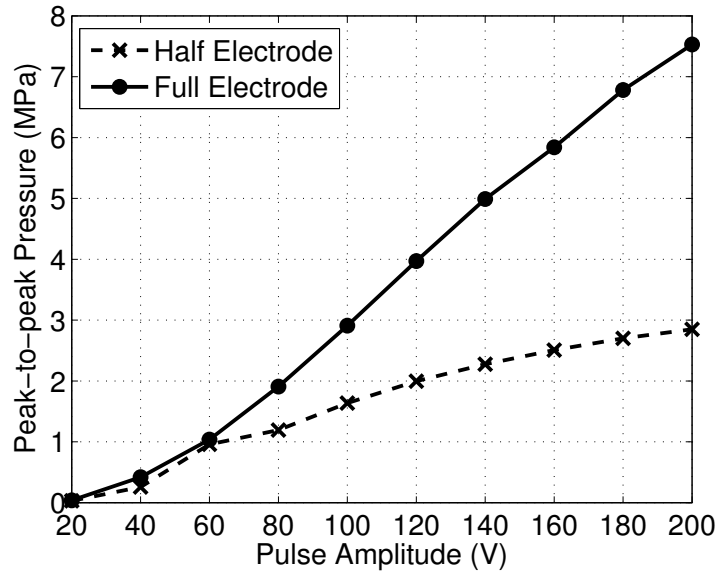


Figure 3.5: Simulated peak-to-peak pressures at the surface of a CMUT when excited by a 40 ns long negative pulses for half electrode and full electrode coverage. The pulse is applied on top of an equal amplitude DC bias and increased step by step. CMUT parameters: $a = 30 \mu\text{m}$, $t_m = 1.4 \mu\text{m}$, $t_g = 0.2 \mu\text{m}$, $t_i = 0.4 \mu\text{m}$.

Considering the transmit efficiency all the analysis in this thesis is done over a full electrode CMUT structure.

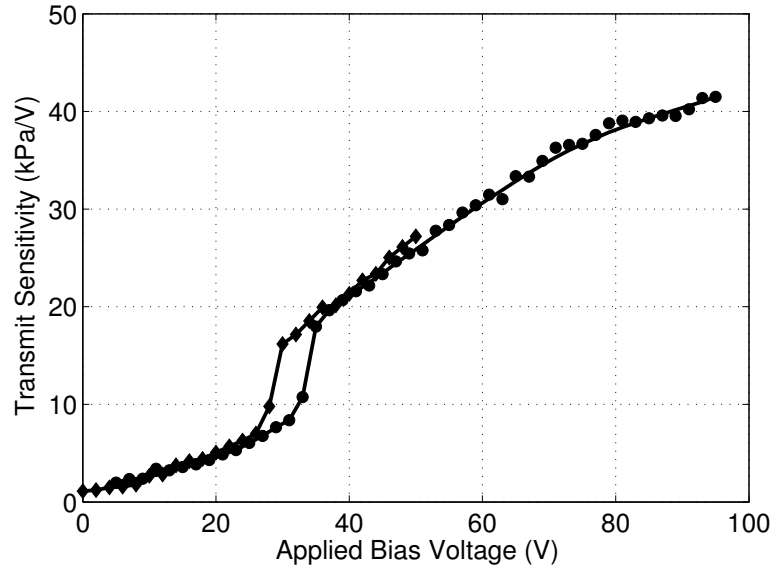


Figure 3.6: Transmit sensitivity of CMUT operated in deep collapse mode. Excited by a 40 ns long, 5-V pulse while the bias is being monotonically increased (circles) and monotonically decreased (diamonds). The sudden jump in the figure is a result of transition stage between collapsed and uncollapsed states. CMUT parameters: $a = 30 \mu\text{m}$, $t_m = 1.4 \mu\text{m}$, $t_g = 0.2 \mu\text{m}$, $t_i = 0.4 \mu\text{m}$.

Chapter 4

Nonlinear Electrical Circuit Model

CMUT as a structure consist of many dependent parameters which makes the optimization difficult. For example, a selected parameter to operate CMUT at a specific frequency, on the other hand affects the operating voltage. The design for a high power CMUT requires an optimization considering all input parameters. Currently, CMUT can be simulated realistically using FEM tools. However, these tools are too much time consuming especially in simulation of larger CMUT arrays under fluid loading. The increased node number for an accurate FEM simulation requires complex mathematical operation of large matrixes in the background and increases the time to simulate the operation. Thus, the optimization of large arrays is practically not possible using FEM tools. The electrical circuit model of the transducer is an alternative to explore the operation. The developed models are lack of nonlinear interactions and are not suitable for large signal excitations. Small signal analysis of the operation is possible but it is not enough for an optimization under large continuous wave signal. Knowing the analytical expressions for membrane deflection under static force and using energy formulations of the capacitance, we developed a nonlinear circuit model which accurately simulates the operation. The missing radiation impedance model of arrays in the previous models is included in order to do a realistic simulation of a CMUT array under fluid loading. In this chapter, we describe our nonlinear large signal model that is used for the optimization in this

thesis.

4.1 The Circuit Model

The circuit model of a CMUT has been widely studied in the past decades. The first developed circuit model was based on Mason's equivalent circuit which conventionally models transducer behaviour [3]. However, the Mason's equivalent circuit is an effective linear model; it only provides small-signal analysis of the transducer under a static DC voltage. The circuit includes a transformer that provides the transition between electrical and mechanical domains. Depending on the applied DC voltage, each time the transformer ratio has to be recalculated and provided to the circuit. On the other hand, it does not include the nonlinear effects and is not suitable for large signal analysis. The first efforts for developing a nonlinear circuit model is proposed by Eccardt et al [37]. It is a 1D model and does not consider the 2D array interaction. A nonlinear circuit model is required to examine the operation of the transducer under different excitations.

FEM tools provide the analysis of CMUT but they are not suitable for optimization in the design stage due to their computational costs. Thus, a large signal nonlinear CMUT model is compulsory for the optimization of CMUT parameters in a fast way.

The nonlinear electrical circuit model of an immersed circular CMUT depicted in Fig. 4.2 is used as the basis of the model in this thesis. The model is created by K. Oguz, et al. in [17, 38] and the performance of the model is demonstrated using a harmonic balance simulator. The model in this thesis is the improved version of this model and it is carried into a SPICE environment in order to do transient simulations. First, the restrictions in the design parameters are eliminated by improving the accuracy of the model. Second, a circuit is created to model the frequency dependent radiation impedance of the array. Previous model assumes that the radiation impedance seen by the array is a real, constant value. But this is not the case in

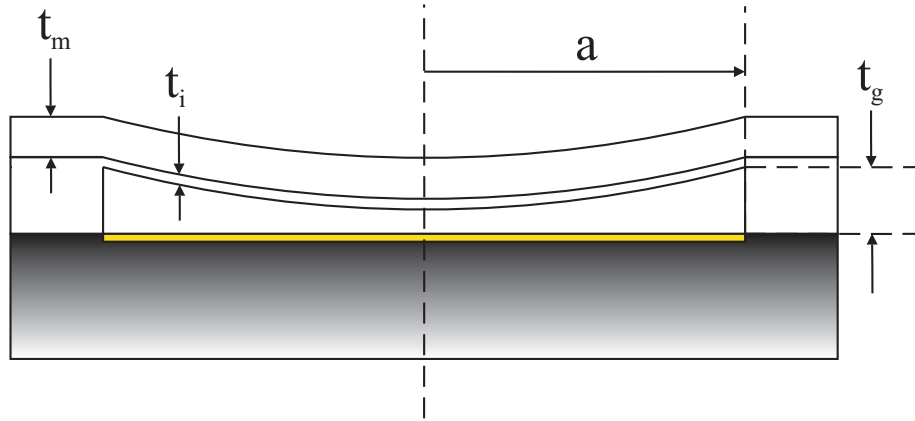


Figure 4.1: Representative cross section of a circular membrane with radius a , thickness t_m and gap height of t_g . Top electrode is the conductive silicon wafer. t_i is the insulating layer thickness above the gap. The bottom electrode is a metal layer.

real. The created R, L, C network accurately models the radiation impedance and provides realistic simulations of the arrays in a fluid medium.

Fig. 4.1 shows the representative cross section of a circular CMUT cell that is modeled in this thesis.

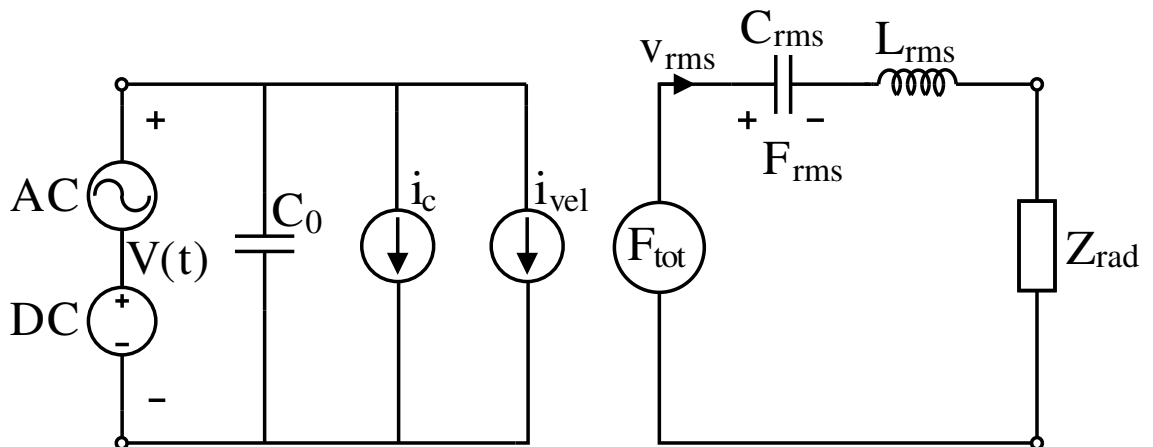


Figure 4.2: Nonlinear equivalent circuit model of a CMUT.

The electrical components of the transducer are at the left side of this circuit. Here, C_0 is the shunt input capacitance of the transducer, and it represents the undeflected membrane capacitance. i_c is the additional nonlinear component of the capacitive current, and i_{vel} is the motion induced current that accounts for the move-

ment of the membrane. The derivations of these two equations are given in [17]. The root mean square (rms) of the velocity distribution on the membrane surface, v_{rms} , is considered as the lumped through variable at the mechanical side of the circuit and is defined as:

$$v_{rms} = \sqrt{\frac{1}{\pi a^2} \int_0^{2\pi} \int_0^a v^2(r) dr d\theta} \quad (4.1)$$

where a is the membrane radius, and $v(r)$ is the velocity of a point at r from the membrane center. The average velocity is not suitable as a lumped variable to determine the kinetic energy of the membrane in a distributed system.

To preserve the kinetic energy of the membrane mass, the mechanical section of the circuit is derived accordingly. Z_{rms} represents the radiation impedance of the CMUT in the model. F_{tot} represents the total force over the membrane in the mechanical domain. L_{rms} and C_{rms} together models the mechanical impedance of the membrane. The membrane is assumed as a first order spring mass system where the mass is modeled by L_{rms} and the inverse of the spring constant (compliance) is modeled by C_{rms} . The details of each component are given in the following sections.

4.2 Membrane Model

The membrane mass is given by

$$L_{rms} = \rho t_m \pi a^2 \quad (4.2)$$

and the compliance of the membrane is given by

$$C_{rms} = 1.8 \left[\frac{16\pi Y_0 t_m^3}{(1 - \sigma^2) a^2} \right]^{-1} \quad (4.3)$$

where the parameters in the equation are listed in Table 4.1. The lumped parameters, L_{rms} and C_{rms} , accurately model the first series resonance frequency of the membrane for $t_m/a < 0.1$ [39].

The membrane velocity profile is modeled quite accurately as a clamped radiator,

$$v(r) = v_p \left[1 - \frac{r^2}{a^2} \right]^n \quad \text{for } r < a \quad (4.4)$$

for $n = 2$, where a is the radius of the membrane, r is the radial position and v_p is the peak velocity at the center of the membrane.

The force and current equations resulting from this velocity profile are derived and the corresponding radiation impedance is employed. However, if t_m/a ratio increases, (4.4) with $n = 2$ begins to match to the velocity profile of the membrane with less accuracy. Thus, this model is not accurate for thick membranes. As L_{rms} defines the mass, it is obvious that a correction is needed for the value C_{rms} value. To improve the accuracy of the membrane model, a correction factor is applied to C_{rms} to make the model accurate for $t_m/a < 0.8$. In order to do that, FEM simulations were done for various membrane radius and thicknesses and a correction factor is used to match the results. With the corrected value, the model with the material properties given Table 4.1 is fully consistent with FEM. The model is also checked for different membrane materials and it is observed that when Poisson's ratio is between 0.2 and 0.35, the error is within 1% percent.

The corrected C_{rms} is as follow

$$C'_{rms} = C_{rms} \left(1.019 + 5.005 \left(\frac{t_m}{a} \right)^{1.981} \right) \quad (4.5)$$

| | |
|---|------------------------|
| Young modulus of Si, Y_0 | 1.3e11 |
| Density of Si, ρ | 2330 |
| Poisson ratio of Si, σ | 0.28 |
| Permittivity of SiO ₂ , ϵ_m | 3.9 |
| Density of water, ρ_0 | 1000 kg/m ³ |
| Speed of sound in water, c | 1500 m/s |

Table 4.1: Membrane material properties used in simulations.

Fig. 4.3 demonstrates the accuracy of the correction term for various values of CMUT dimensions.

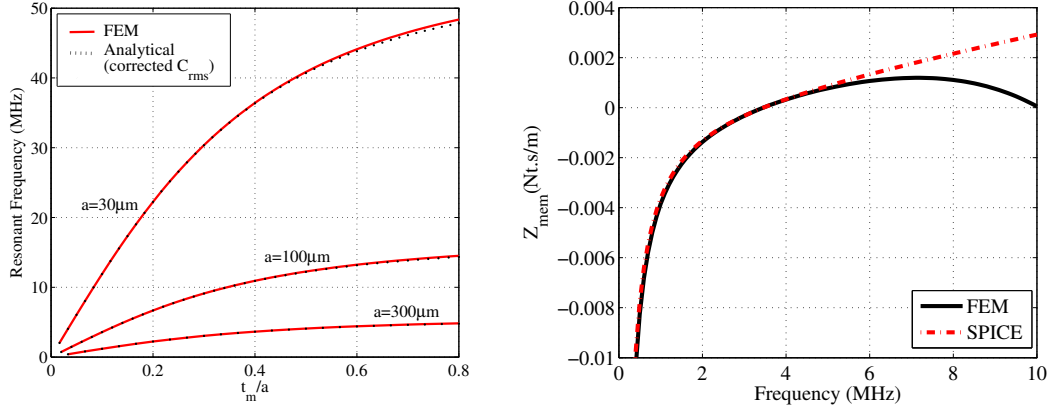


Figure 4.3: The resonant frequency of the membrane as determined from L_{rms} and C'_{rms} for various t_m/a values. C'_{rms} is the corrected capacitor value to accurately model resonant frequency (left). Membrane impedance is plotted for a radius of $280 \mu\text{m}$ and a membrane thickness of $92 \mu\text{m}$ (right).

The membrane impedance is compared with FEM results in Fig. 4.3. The reader should note that the model does not predict higher modes of the membrane, it is accurate up to more than two times the series resonance frequency of the CMUT.

When the membrane area is divided into small rings with an area of $2\pi r dr$, from the principle of virtual work, the force on this small ring is found by differentiating the stored energy in the clamped capacitance with respect to the displacement of the membrane [17, 40].

$$\delta F(r, t) = \frac{d[\delta E_{tot}(r, t)]}{dx} = \frac{1}{2}V^2(t) \frac{d[\delta C(x(r, t))]}{dx} \quad (4.6)$$

where $x(r, t)$ is the membrane displacement normal to the surface and the capacitance of the ring is

$$\delta C(x(r, t)) = \frac{\epsilon_0 2\pi r \delta r}{t_{ge} - x(r, t)} \quad (4.7)$$

where $t_{ge} = t_g + t_i/\epsilon_m$ and ϵ_m is the permittivity of insulating layer.

Total force on the membrane is found by integrating (4.6) as $\delta r \rightarrow 0$ and the result is found to be

$$F_{tot}(t) = \frac{C_0 V^2(t)}{4t_{ge}} \left[\frac{t_{ge}}{t_{ge} - x_p(t)} + \frac{\tanh^{-1}\left(\sqrt{\frac{x_p(t)}{t_{ge}}}\right)}{\sqrt{\frac{x_p(t)}{t_{ge}}}} \right] \quad (4.8)$$

where $C_0 = \epsilon_0 \pi a^2 / t_{ge}$. The ϵ_0 is the free space permittivity.

4.3 Nonlinear Currents, i_c and i_{vel}

The charge on each ring over the membrane can be written as

$$\delta Q(r, t) = V(t) \delta C(x(r, t)) \quad (4.9)$$

The time derivative of the charge gives the current,

$$\frac{d}{dt}[\delta Q(r, t)] = \delta C(x(r, t)) \frac{dV(t)}{dt} + \frac{d[\delta C(x(r, t))]}{dt} V(t) \quad (4.10)$$

Integrating 4.10 as $\delta r \rightarrow 0$ results in two current components. The integral of the term at the left side of 4.10 is

$$I_{left} = C_0 \frac{dV(t)}{dt} \left[\frac{\tanh^{-1} \left(\sqrt{\frac{x_p(t)}{t_{ge}}} \right)}{\sqrt{\frac{x_p(t)}{t_{ge}}}} \right] \quad (4.11)$$

where the $C_0 \frac{dV(t)}{dt}$ is the current passing over the C_0 in the circuit. Thus, the nonlinear component of this term can be separately written as

$$i_c = C_0 \frac{dV(t)}{dt} \left[\frac{\tanh^{-1} \left(\sqrt{\frac{x_p(t)}{t_{ge}}} \right)}{\sqrt{\frac{x_p(t)}{t_{ge}}}} - 1 \right] \quad (4.12)$$

which is called as nonlinear capacitive current, i_c . On the other hand, the integral of the term at the right side of 4.10 is

$$I_{right} = i_{vel} = \frac{C_0 V(t)}{2x_p} \frac{dx_p(t)}{dt} \left[\frac{t_{ge}}{t_{ge} - x_p} - \frac{\tanh^{-1} \left(\sqrt{\frac{x_p(t)}{t_{ge}}} \right)}{\sqrt{\frac{x_p(t)}{t_{ge}}}} \right] \quad (4.13)$$

This second nonlinear current is a result of membrane motion and it is denoted as i_{vel} .

4.4 Radiation Impedance

When CMUT operates in a fluid medium, the circuit must be terminated by a radiation impedance component. The radiation impedance seen by a CMUT or an array is not purely real and has imaginary components. It is frequency dependent and it is a strong function of ka product. For the array case, it also depends on the number of CMUT cells and their positions in the array (Fig. 4.4) [41]. The radiation impedance can be modeled by using RLC circuit components in a parametric manner [42]. The component values are defined in terms of the membrane radius, a , the sound velocity in the medium, c , the density of the medium, ρ_0 and the number of cells in the array (N). The model accurately mimics the radiation impedance in any case of a change in the related parameters.

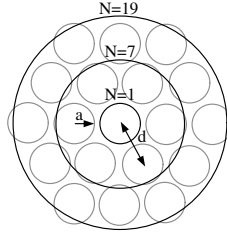


Figure 4.4: The configuration of CMUT array for different number of cells.

To model the radiation impedance of a single CMUT cell, the circuit in Fig. 4.5 is proposed. The circuit accurately models the radiation impedance of a single cell (Fig. 4.6). The component values of the circuit for the normalized radiation impedance is given in Table 4.2.

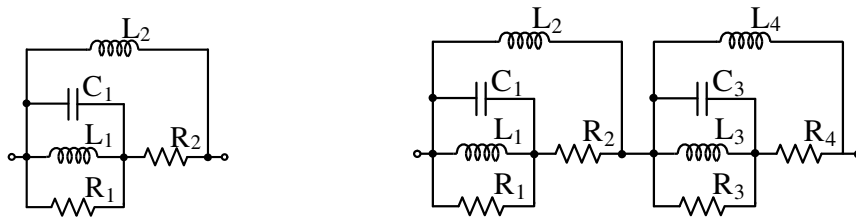


Figure 4.5: RLC model for the normalized radiation resistance and reactance of a single CMUT cell (left) and an array of CMUT (right).

To model the radiation impedance of an array of CMUT cells, the subcircuit is

repeated in series as in Fig. 4.5. The proposed circuit models the radiation impedance of CMUT arrays with 7 and 19 cells. For different number of cell configurations, the component values are also given in Table 4.2.

| N | 1 | 7 | 19 |
|-----------|------------|------------|------------|
| R_1/R_n | 0.64 | 0.39 | 0.48 |
| L_1/R_n | 0.54 a/c | 0.55 d/c | 1.2 d/c |
| C_1R_n | 0.2 a/c | 1.38 d/c | 1.22 d/c |
| R_2/R_n | 0.90 | 0.02 | 1.4e-6 |
| L_2/R_n | 0.37 a/c | 0.77 d/c | 2.3 d/c |
| R_3/R_n | — | 1.31 | 2.06 |
| L_3/R_n | — | 0.07 d/c | 0.05 d/c |
| C_3R_n | — | 0.32 d/c | 0.40 d/c |
| R_4/R_n | — | 1.04 | 1.12 |
| L_4/R_n | — | 0.28 d/c | 0.29 d/c |

Table 4.2: Component values for the radiation impedance model with different number of cells in the array where $R_n = \pi a^2 \rho_0 c / N$.

A smaller circuit is sufficient to model the radiation of a single CMUT cell. The accuracy of the model is demonstrated in Fig. 4.6 for $N=1$, 7 and 19, respectively. The R, L values are multiplied and C values are divided by R_{norm} to form the actual radiation impedance, Z_{rms} , of the element in the circuit, where R_{norm} is $\pi a^2 \rho_0 c$.

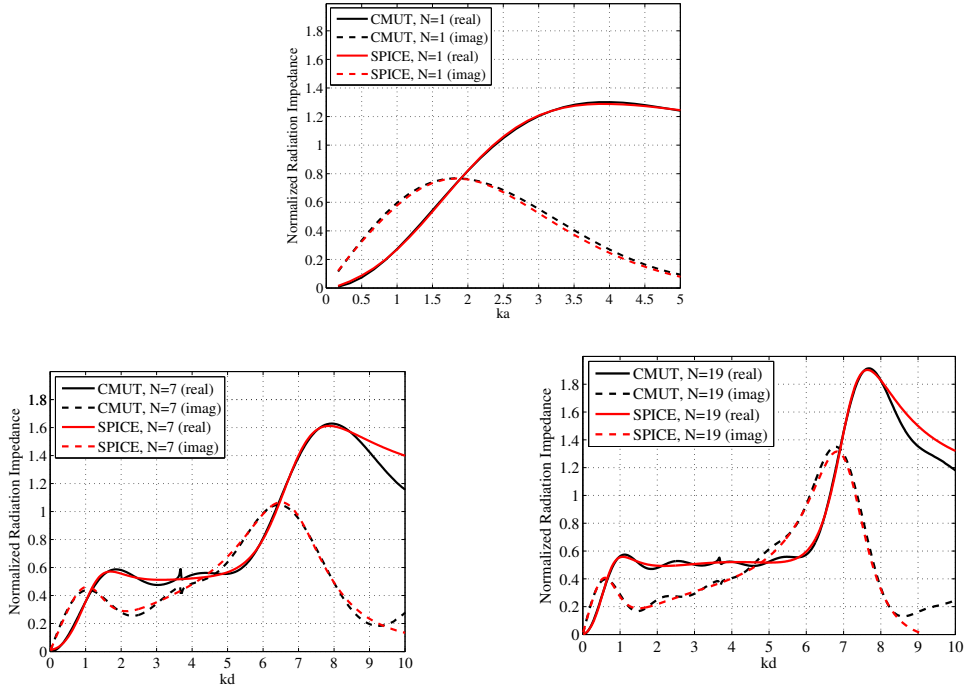


Figure 4.6: The normalized radiation impedance of a single CMUT (top) and a CMUT array of 7 cells (left) and 19 cells (right) with the RLC model and actual values.

4.5 Modeling Nonlinear Components in SPICE

The circuit is created in a public domain circuit simulator, LTSPICE (Linear Technology Spice Simulator)¹. The simulation environment is suitable to create a circuit component with user defined variables. The tool also allows the sweeping of any defined parameters or an input for the simulation. Furthermore, it creates flexible environment to optimize the parameters.

Each component value in the simulator is defined parametrically in terms of the CMUT geometry and its properties.

Behavioral sources are used to generate the main components in the circuit. To model i_c and i_{vel} , “behavioral current sources” are used. F_{tot} is modeled using a “behavioral voltage source”. These components are all require x_p as input, thus a

¹LTSPICE, <http://www.linear.com/designtools/software> (Linear Technology, CA, USA).

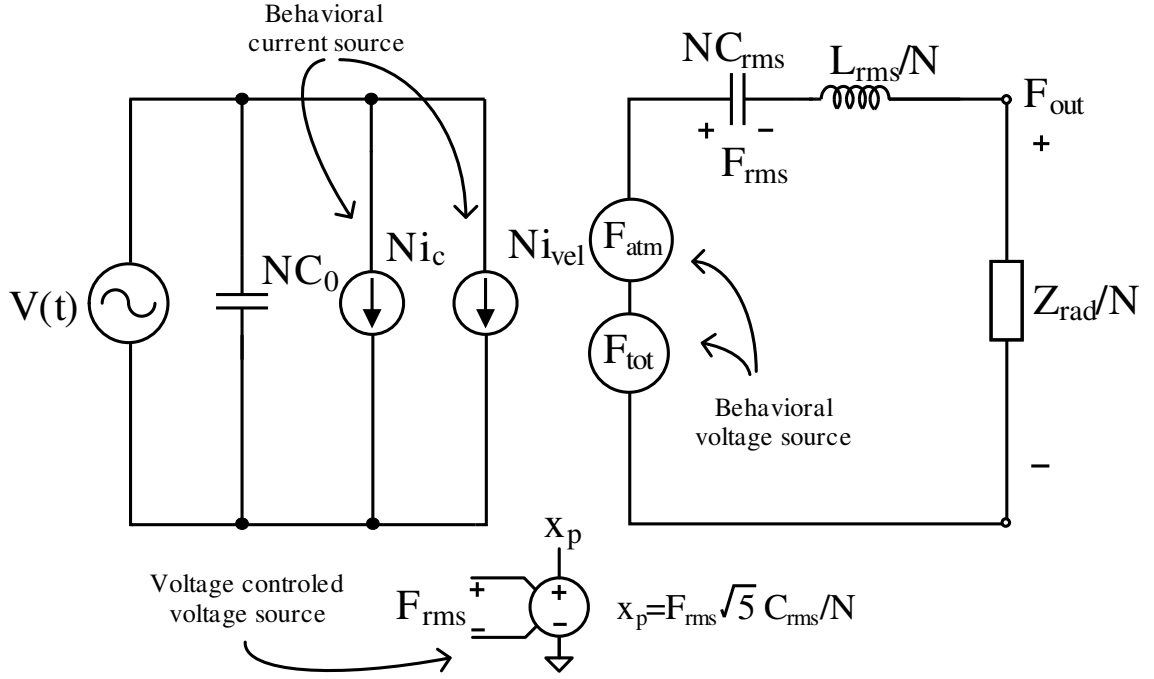


Figure 4.7: SPICE Model. The radiation impedance is modeled by R, L, C circuit components. N represents the number of cells in the array.

small subcircuit is also created with a voltage controlled voltage source to generate x_p .

The RMS displacement x_{rms} is equal to the charge on C_{rms} , which can be calculated as

$$v_{rms} = \frac{dx_{rms}}{dt} = C_{rms} \frac{dF_c}{dt} = \frac{dQ_c}{dt} \quad (4.14)$$

When this value is multiplied with $\sqrt{5}$, the peak displacement at the center of the membrane (x_p) is obtained [17].

$$x_p = \sqrt{5} C_{rms} F_c \quad (4.15)$$

The small subcircuit does the work described above. Alternatively, x_p value can be obtained by taking the integral of the current, v_{rms} , and multiplying with $\sqrt{5}$ using a behavioral voltage source. The surface pressure is calculated by dividing the

force over the radiation impedance, F_{out} , to the surface area of the CMUT cell.

When CMUT operates in air, the effect of atmospheric pressure must be included in the model. The effect can be easily included in the model by adding an extra force term into the total force equation at the mechanical side. This force term is written in terms of the atmospheric pressure multiplied by the surface area and the rms correction factor [17].

$$F_{atm} = \frac{\sqrt{5}}{3} P_{atm} \pi a^2 \quad (4.16)$$

The model is first tested for operation in vacuum. In that case, the radiation impedance seen by the CMUT is zero. So, the radiation impedance component is not included in the model and that section of the circuit is shorted.

x_p values predicted for different DC voltages are in good agreement with FEM results as shown in Fig. 4.8.

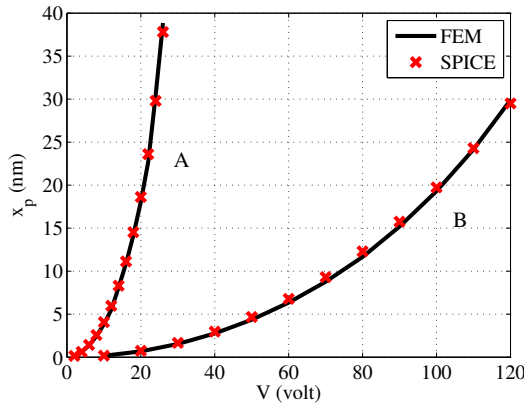


Figure 4.8: The static deflection of membrane center as calculated by FEM and the circuit model ($a = 30 \mu\text{m}$, $t_m=2 \mu\text{m}$, $t_i=0.1 \mu\text{m}$, $t_g=0.1 \mu\text{m}$ (A). $a = 300 \mu\text{m}$, $t_m=100 \mu\text{m}$, $t_i=0.4 \mu\text{m}$, $t_g=0.1 \mu\text{m}$ (B).)

The transient performance of the circuit model is tested in air. The center displacement of the membrane, x_p , is compared with the FEM result in Fig. 4.9.

After verifying the circuit performance of single CMUT operating in vacuum. The radiation impedance of a single cell is included by replacing the proposed RLC

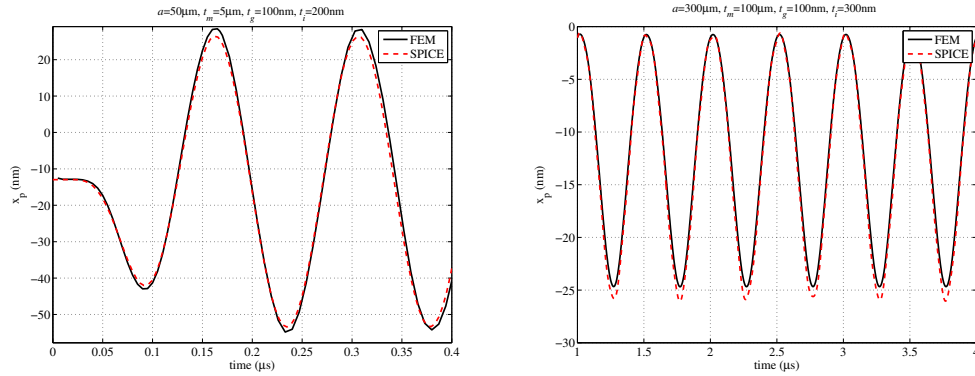


Figure 4.9: Single CMUT cell in vacuum. 1 cycle 20V AC voltage at 7.3 MHz with 20V DC voltage (left) and 4 cycle 100Vpeak cosine burst at 1 MHz (right) is applied.

circuit to the radiation impedance section. A 100 V peak 2-cycle burst sinusoidal signal is applied to a single CMUT model in water. As seen from the Fig. 4.10, the circuit model accurately simulates the CMUT operation. Lastly, the model is tested for a CMUT array of seven cells. The 3D FEM model, described in the appendix, is used to simulate the surface pressure of the element. The observed surface pressures are compared in Fig. 4.11. The difference in the peak pressure is due to the difference in the predicted radiation impedance by the 3D FEM Model. The FEM model takes around 30 hours for the 4 μ s transient analysis of the element, whereas the created circuit model takes less than a second for the same simulation.

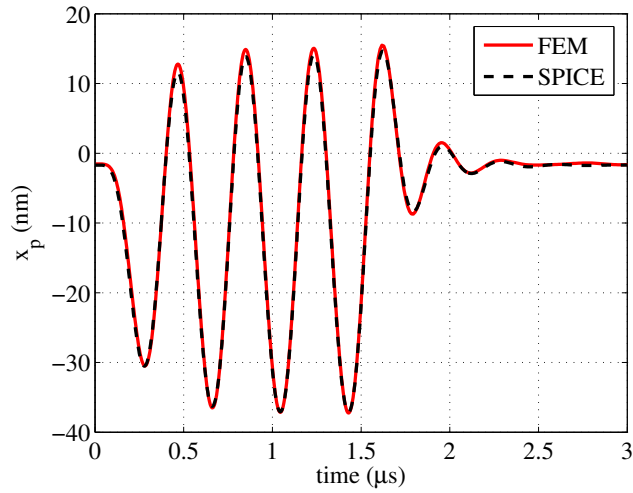


Figure 4.10: 2 cycle 100Vpeak cosine burst at 1.3 MHz is applied to a single CMUT under fluid loading ($a=300 \mu\text{m}$, $t_m=100 \mu\text{m}$, $t_g=100 \text{nm}$, $t_i=400 \text{nm}$.)

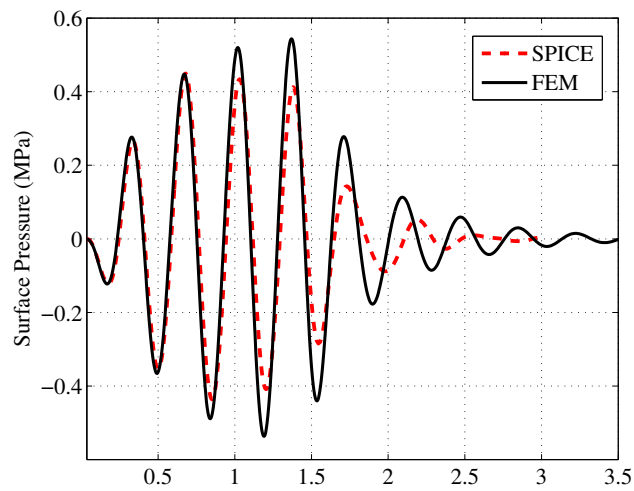


Figure 4.11: Observed surface pressure. 2 cycle 100Vpeak cosine burst at 1.44 MHz is applied to CMUT element with 7 cells under fluid loading ($a=280 \mu\text{m}$, $t_m=92 \mu\text{m}$, $t_g=110 \text{nm}$, $t_i=350 \text{nm}$.)

Chapter 5

Optimization of CMUT Parameters for HIFU

This chapter introduces the methodology to design a CMUT array for HIFU operation. Using the nonlinear circuit model described in the previous chapter, we propose a methodology to design and operate CMUTs for a specific HIFU operation. The operating frequency of the application and the available input voltage levels are defined as the constraints of this optimization. The flowchart of the optimization is given and a guideline is created. For maximum power delivery to the medium, we targeted an operation where the radiation resistance seen by the array is at the maximum.

5.1 Operating at half the resonance frequency

Conventionally, transmitting CMUTs are excited with a sinusoidal signal on a DC bias voltage. DC voltage may cause charging in the insulating layer [43]. The trapped charges drift the voltage and shifts the operating frequency [44]. Hence, it causes a degradation in the CMUT performance. It is important to eliminate charging when a repeatable CMUT operation is critical.

For a CMUT operating under a continuous wave signal, it is possible to eliminate the DC voltage at the input. This can be done by applying a sinusoidal signal with a frequency at half of the operating frequency. If the applied drive voltage is

$$V(t) = V_{max} \cos\left(\frac{\omega}{2}t + \theta\right) \quad (5.1)$$

where V_{max} is the peak voltage, then F , the force on the membrane, will be proportional to

$$F \propto V^2(t) = \frac{V_{max}^2}{2} [1 + \cos(\omega t + 2\theta)] \quad (5.2)$$

As seen in Eq. 5.2, $V^2(t)$ includes a DC term that will naturally form a bias voltage and a sinusoidal force term at the operating frequency. Therefore, the mechanical effect of the DC voltage can be achieved by using a continuous wave signal at half of the operating frequency.

The optimization in this work is done for driving the CMUTs at the half the resonance frequency, so that DC voltage is eliminated which causes charge trapping in the insulating layer and degrades the CMUT performance.

5.2 Optimization

We start the optimization by defining an initial boundary for the maximum operating voltage. This voltage is assumed to be the maximum available input voltage and insulating layer thickness is defined accordingly. The selected insulator thickness, t_i , should prevent the breakdown during the operation. We assumed that our maximum operating voltage is 100V and the insulating layer is chosen as silicon dioxide with a thickness of $t_i=200$ nm for a safe operation.

We assumed that our target operating frequency is 3 MHz and we are going to use an array configuration of 7 cells. The radiation impedance peak of such an array is at $ka = 3.75$. Thus, the radius to observe the maximum radiation impedance at this frequency is $298.4\mu\text{m}$. Using the circuit model, we swept the t_m parameter

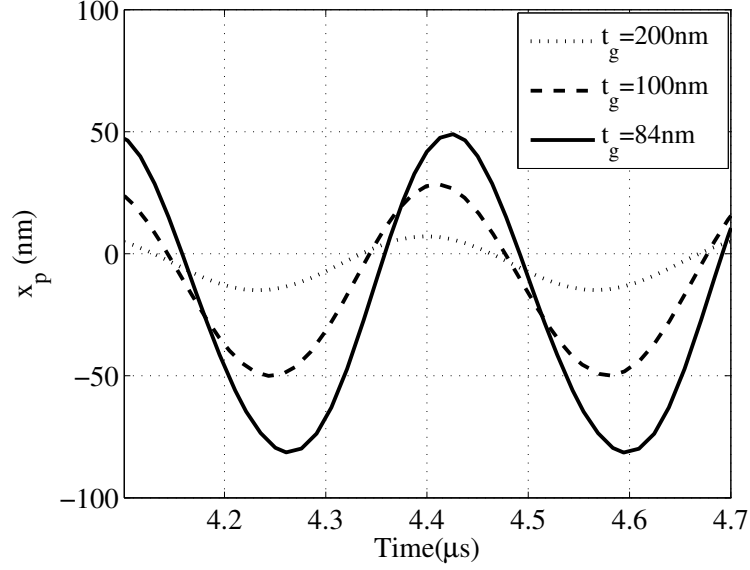


Figure 5.1: The center displacement of the membrane for different t_g under a continuous 100V 1.5MHz sinusoidal signal ($a=289.5 \mu\text{m}$, $t_m=130 \mu\text{m}$, $t_i=100 \text{nm}$).

to find the required membrane thickness for a resonance at 3 MHz. t_m is found as $130 \mu\text{m}$. After the resonance frequency is set, $100V_p$ continuous cosine signal at half the resonant frequency (1.5 MHz) is applied to the circuit. t_g is reduced from a high value down to a height where the center of the membrane is about to touch the bottom electrode during the operation. At a t_g value of 84 nm the center peak displacement reaches 80 nm (Fig. 5.1). At this point, the resonance frequency shifts due to the spring softening. In order to adjust the resonance frequency, the membrane thickness is increased and the last step is repeated. After a few iterations, t_m and t_g values converge to $125 \mu\text{m}$, 81 nm, respectively.

For a known operating frequency and given peak voltage, the optimization flow chart is given in Fig. 5.2

Table 5.1 lists the optimized CMUT parameters for continuous 3 MHz operation. As seen from the table, the CMUT operating at the peak of the radiation impedance provides the maximum pressure with the lowest second harmonic.

| $a(\mu m)$ | ka | $t_m(\mu m)$ | $t_g(\text{nm})$ | $x_{p-p}(\text{nm})$ | Surface Pressure (MPa) | 2nd Harmonic (dB) |
|------------|------|--------------|------------------|----------------------|------------------------|-------------------|
| 20 | 0.25 | 1.6 | 168 | 175 | 1.24 | -11 |
| 50 | 0.62 | 6 | 132 | 140 | 1.32 | -12 |
| 100 | 0.62 | 25 | 95 | 128 | 3.6 | -21 |
| 298.5 | 3.75 | 130 | 84 | 128 | 3.02 | -27 |
| 350 | 4.4 | 170 | 80 | 112 | 2.7 | -25 |

Table 5.1: Design Comparisons at 3 MHz. ($t_i=200$ nm, $N=7$, $100 V_p$,)

The available input voltage changes the results dramatically. When the available voltage is increased up to 200V ($t_i=400$ nm), the surface pressure reaches 4.3 MPa with harmonics at -27dB for the optimum design which is not possible with the current PZT technology.

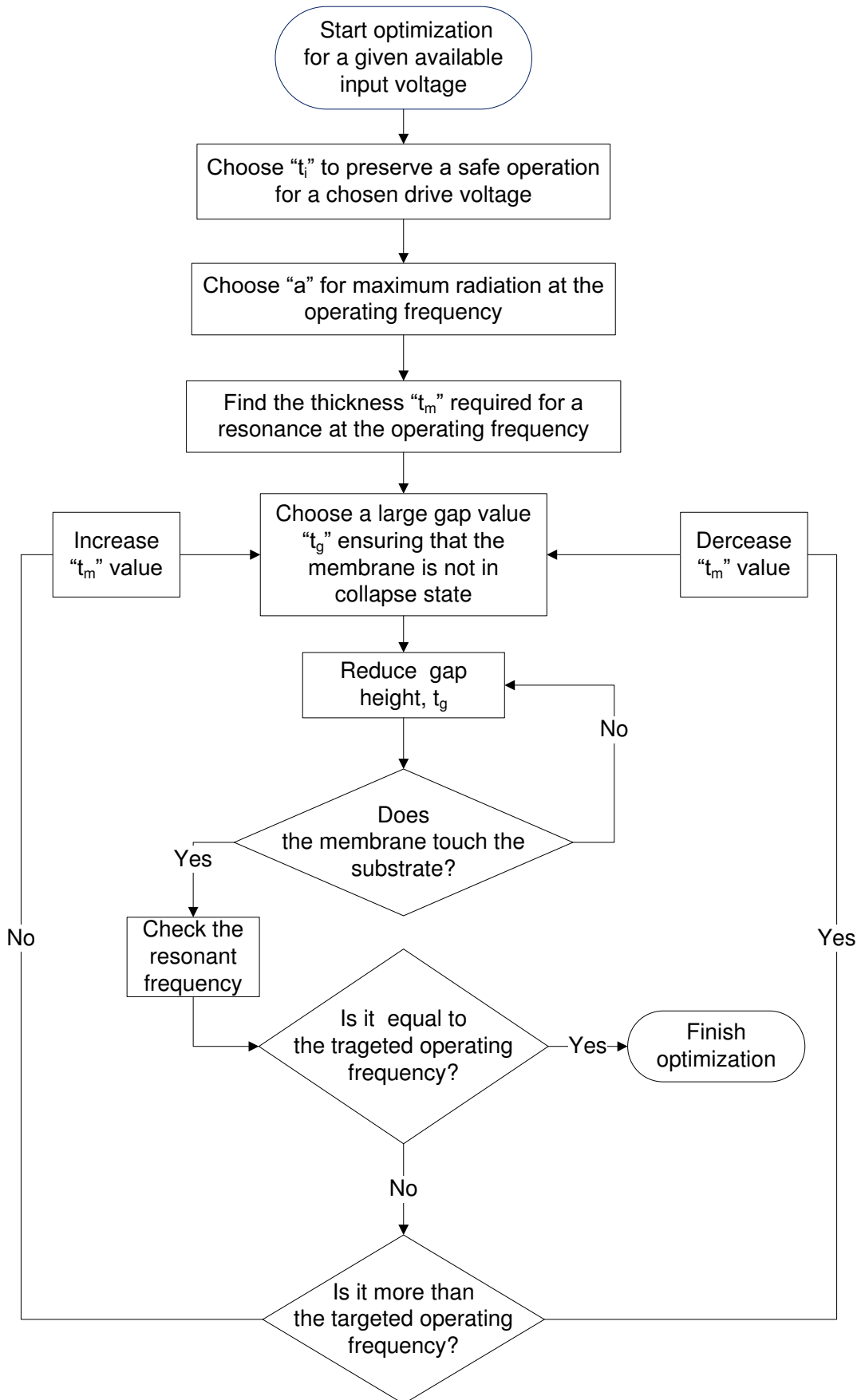


Figure 5.2: The flowchart of the optimization.

Chapter 6

Fabrication

Conventionally, CMUTs are fabricated using sacrificial release process in which a cavity is formed by removing the sacrificial layer [7, 45–48]. Sealing is required to vacuum cavity in this process after removing the sacrificial layer through the etch holes. The typical membrane thickness is around a few microns and the sacrificial layer thickness defines the cavity height. Recently, CMUTs are started to be fabricated using wafer bonding technology [9, 49, 50]. The technology enables more control over the process. Gap height can be defined precisely. Moreover, the membrane thickness is no more limited by the deposition; the wafer itself is used as a membrane or a predefined membrane layer is transferred. For the fabrication of a high power CMUT transducer, we utilized anodic wafer bonding technology. Anodic bonding is used to bond a silicon wafer to a borosilicate wafer using proper pressure, electric field and temperature. The cavities and the insulating layer are formed over the silicon wafer and the bottom electrode is defined over the borosilicate wafer. The process for each side is explained in detail.

6.1 Membrane Side

We defined the cavity of the CMUTs on the silicon side 6.1. The microfabrication process on the silicon side starts with a 3 inches, highly doped, double side polished silicon wafer. High conductivity of this wafer (0.015-0.020 ohm-cm) serves as one of the electrodes of the CMUTs. The thickness of the silicon wafer determines the thickness of the membrane. The wafer thickness is measured as $92\ \mu\text{m}$ using surface profiler. First, an insulation layer of 450 nm silicon oxide is thermally grown in a diffusion furnace. The silicon wafer is kept in the furnace at 1050°C for one hour in the presence of adequate water vapor. Second, 100 nm of silicon oxide is etched using a reactive ion etching (RIE) reactor to create the cavities. As the last process on the silicon side, the silicon oxide at the back side of the silicon wafer is etched away using the RIE reactor to get an electrical contact.

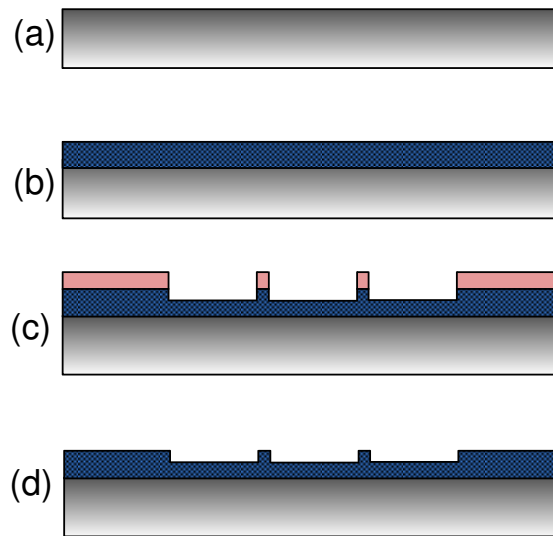


Figure 6.1: (a) 3 inch Conductive silicon wafer with a thickness of $100\ \mu\text{m}$. (b) Thermal oxidation (c) Lithography and oxide etching to form the cavities



Figure 6.2: The photograph of the completed process on membrane side.

6.2 Substrate Side

Having completed the membrane side, the substrate side is fabricated on a 3.2 mm thick 4 inches borosilicate wafer (Fig. 6.3). The substrate wafer is chosen to be quite thick in order to maintain a rigid substrate. Since the smoothness of the borosilicate surface is critical for the success of the anodic bonding, the substrate electrode is buried on the glass wafer. An image reversal photoresist (AZ5214E) is used for the lift-off process. Before the evaporation of the gold electrode, the glass is etched approximately by the thickness of gold to be evaporated. As the substrate electrode, 15 nm of titanium and 85 nm of gold are deposited by thermal evaporation. The borosilicate and silicon wafers are cleaned at 120°C in Piranha etch (1:3 H₂O₂:H₂SO₄) for 15 minutes before the bonding process. The prepared wafers are then anodically bonded¹. The current passing during the bonding process is limited to prevent dielectric breakdown, since a bonding voltage up to 1000V is utilized.

Since the borosilicate wafer is larger than the silicon wafer, the substrate electrical contacts are taken at the exposed gold electrodes on the surface of the borosilicate wafer 6.5. Electrical contacts are made using a silver conductive epoxy². A photograph of the completed fabrication is seen in Fig. 6.6.

¹Applied Microengineering Ltd, Oxfordshire, UK.

²Eccobond 83C (Emmerson-Cumming)

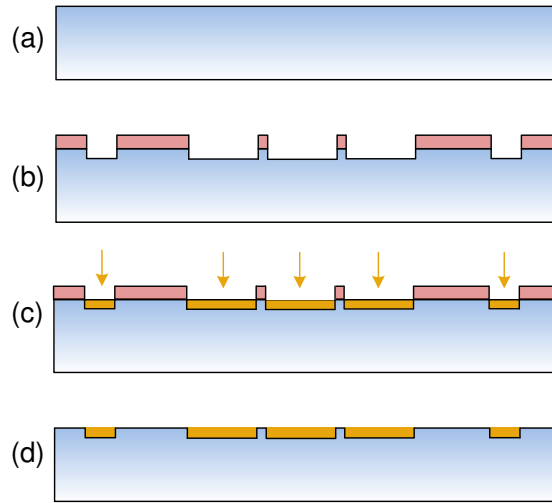


Figure 6.3: (a) Borosilicate glass wafer (b) Lithography and glass etching for bottom electrode (c) Ti/Au deposition (d) Cleaning

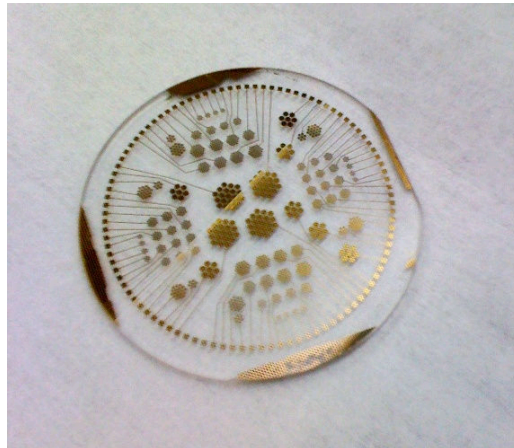


Figure 6.4: The photograph of the completed process on glass side.

6.3 Fabricated Devices

For testing purposes, we included different types of arrays in the fabrication mask. As the thickness of the membrane is fixed by the silicon wafer itself, we created arrays with different membrane radiuses. The properties of the fabricated CMUTs are given in Table 6.1.

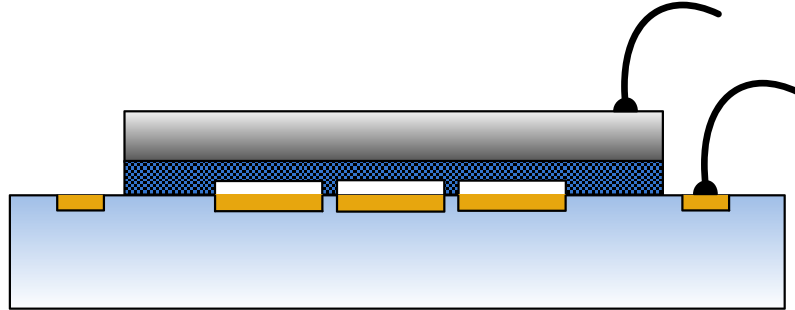


Figure 6.5: After anodic bonding, lead wires are connected using conductive epoxy.

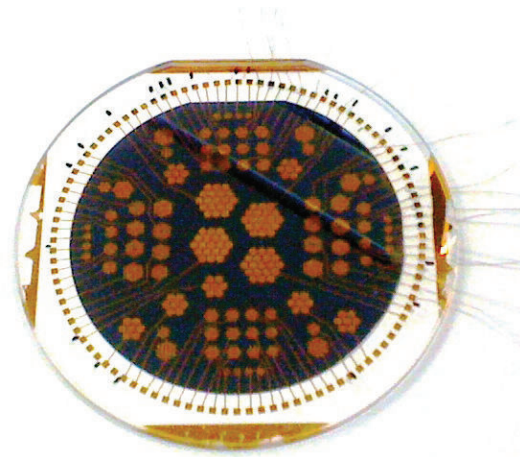


Figure 6.6: Fabricated CMUTs.

| | |
|---------------------------------|---------------------------------------|
| Membrane material | Si |
| Membrane thickness | 92 μm |
| Membrane radius | 260/280/300/320/450/900 μm |
| Insulating layer thickness | 350 nm |
| Cavity height | 110 nm |
| Number of cells in the elements | 7/19/39 |

Table 6.1: Properties of the fabricated devices.

Chapter 7

Measurements

After fabrication, the fabricated devices are tested. First, the predicted operating frequencies are compared with the measurements. As fabricated devices has a silicon wafer thickness of $92\ \mu\text{m}$, we observed the maximum radiation resistance with the array radius of $280\ \mu\text{m}$ that operates at 3 MHz. The immersion measurements are done in the vegetable oil with the CMUT array of 7 cells. The tested array has a ka value of 3.56.

7.1 Impedance measurements in air

To verify that CMUTs are working, CMUTs are connected to the HP E5071C network analyzer. The impedance measurements were done over different fabricated elements to check the resonant frequencies in air (Table 7.1).

The tested CMUT element properties is given in Table 7.2. The element consists of 7 CMUT cells. HP 4284A LCR meter is used for capacitance measurement and the total capacitance including the paths is measured as 103 pF.

| Radius | Resonant frequency (air) |
|-------------------|--------------------------|
| 260 μm | 3.2 MHz |
| 280 μm | 3 MHz |
| 300 μm | 2.6 MHz |
| 320 μm | 2.3 MHz |

Table 7.1: Resonant frequencies in air.

7.2 Immersion Experiments

Immersion experiments were done in a vegetable oil tank (Fig. 7.1). The setup in Fig. 7.2 is used for characterizing the transmit mode of operation of the fabricated CMUTs.

Signal generator output is amplified by using ENI 2100 100W Class A Linear Power amplifier. The amplifier has a fixed nominal gain of 50 dB. The amplified 5 cycle cosine burst signal at 1.44 MHz is applied to the transducer element. An HGL-200 calibrated ONDA hydrophone is placed 1 cm away from the transducer surface. The AH-2010 preamplifier is connected to the hydrophone with ONDA AR-AMAF connector. The measured signal is first corrected for the diffraction and attenuation losses ¹ to obtain the pressure generated on the radiation resistance at the surface. This pressure is further modified using the radiation impedance given in Fig. 4.6 to obtain the total pressure on the surface of the transducer. Latter modification is exact for the fundamental component at 2.88 MHz and since the signal has low harmonic content (second harmonic < 25 dB), the contribution due to errors in

¹Attenuation in sun flower oil, $\alpha = 5.68e^{-12} \text{ m}^{-1}\text{Hz}^{1.85}$ [51]

| | |
|------------------------------------|---------------------------|
| membrane radius, a | 280 μm |
| membrane thickness, t_m | 92 μm |
| insulating layer, thickness, t_i | SiO ₂ , 350 nm |
| gap height, t_g | 110 nm |

Table 7.2: The parameters of the tested CMUTs on glass wafer.

harmonics are insignificant. The measured surface pressures for the applied peak voltages is given in Fig. 7.3.

When the membrane gets closer to the bottom electrode, the attractive force increases due to the increased electrical field. Thus, the velocity profile changes and the nonlinearity increases. On the other hand, the energy that is stored to move the membrane in the other direction is released by the mechanical movement of the membrane which is more linear. It can be easily seen that the positive peaks of the pressure is more sinusoidal as a result of the resonance (Fig. 7.3). For the operation, the tradeoff between second harmonic and the peak pressure should be carefully considered (Fig. 7.4).

1.8 MPa peak to peak pressure with -28 dB second harmonic is measured at the transducer surface for a peak voltage of 125V (Fig. 7.6). Due to the load impedance of the CMUT which is directly connected to the power amplifier, this voltage is measured as the maximum applicable voltage.

7.3 Model Validation

The parameters of the fabricated CMUT are directly entered to the SPICE model and surface pressure is compared to the measurement result. SPICE model predicts 1.7 MPa peak to peak surface pressure for the same peak voltage and the pressure can be increased up to 2.5 MPa with a maximum peak voltage of 145V. On the other hand, 1.2 MPa with -32 dB is observed for a peak voltage of 100V.

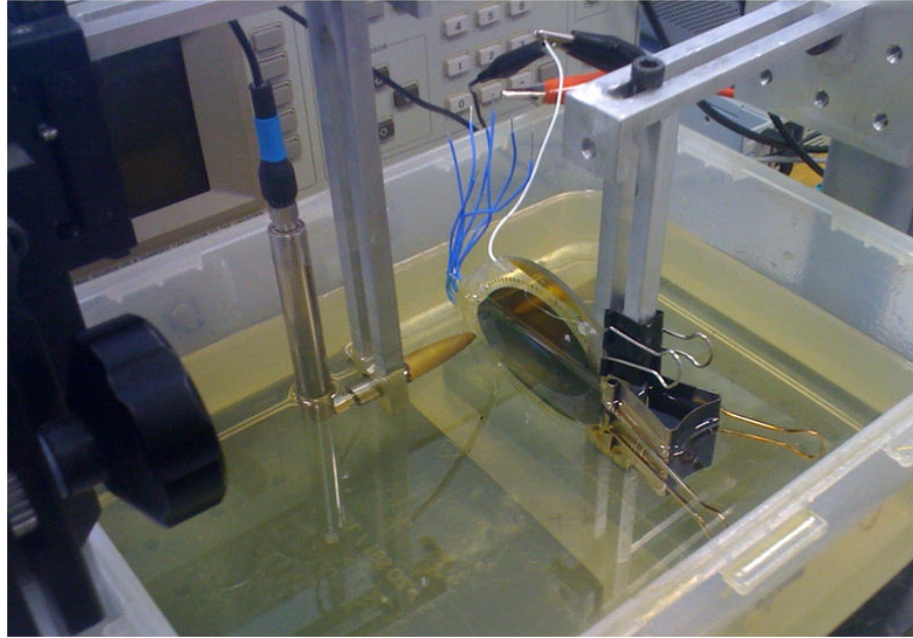


Figure 7.1: Picture of the experimental setup.

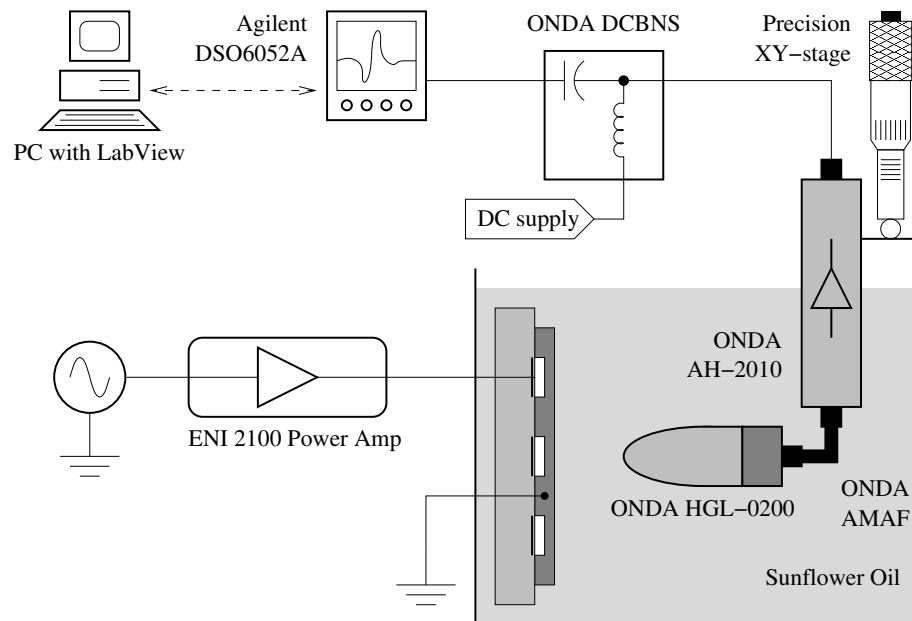


Figure 7.2: Schematic of the experimental setup with the devices.

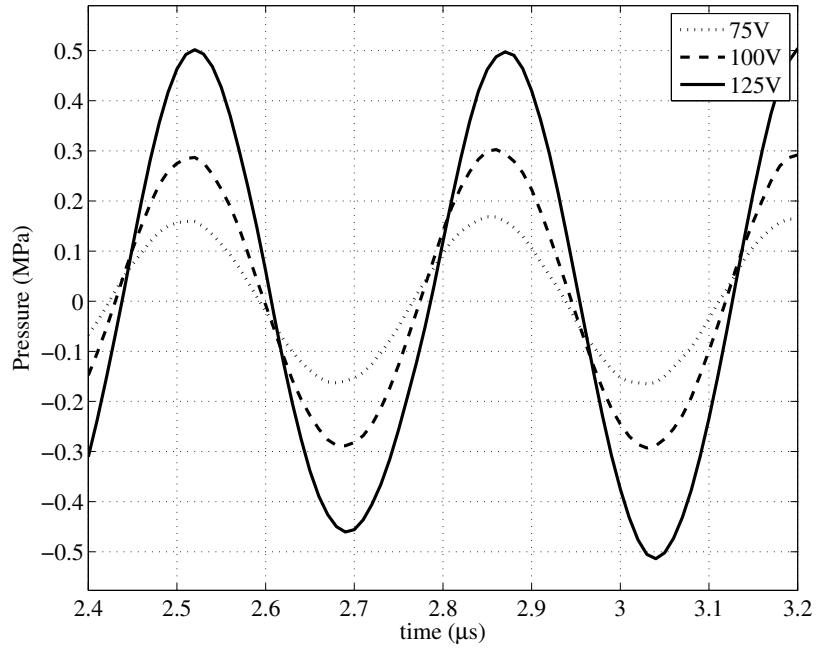


Figure 7.3: Measured surface pressures for different peak voltages at 1.44 MHz.

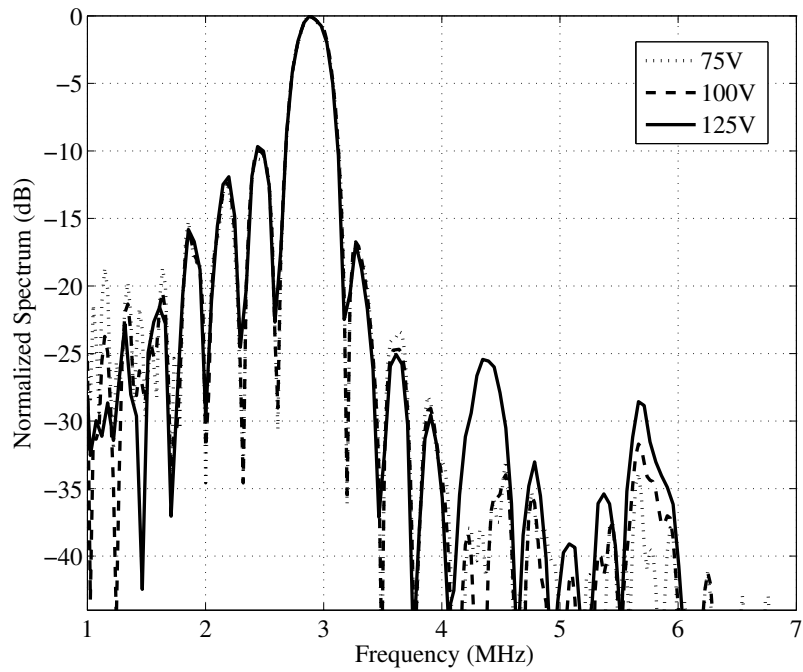


Figure 7.4: Normalized frequency spectrum of the surface pressure for different peak voltages.

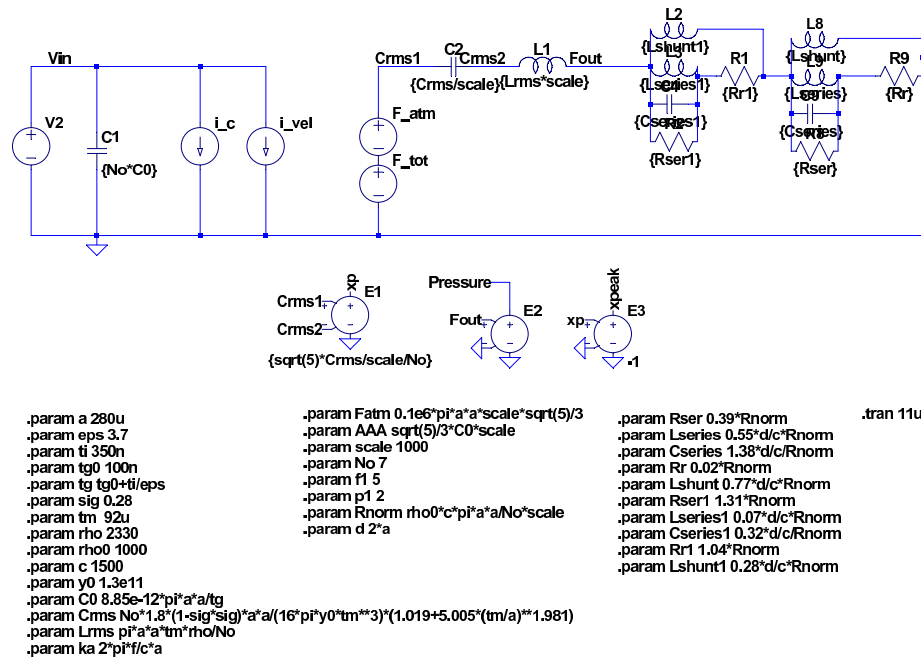


Figure 7.5: The SPICE model with the fabricated device parameters.

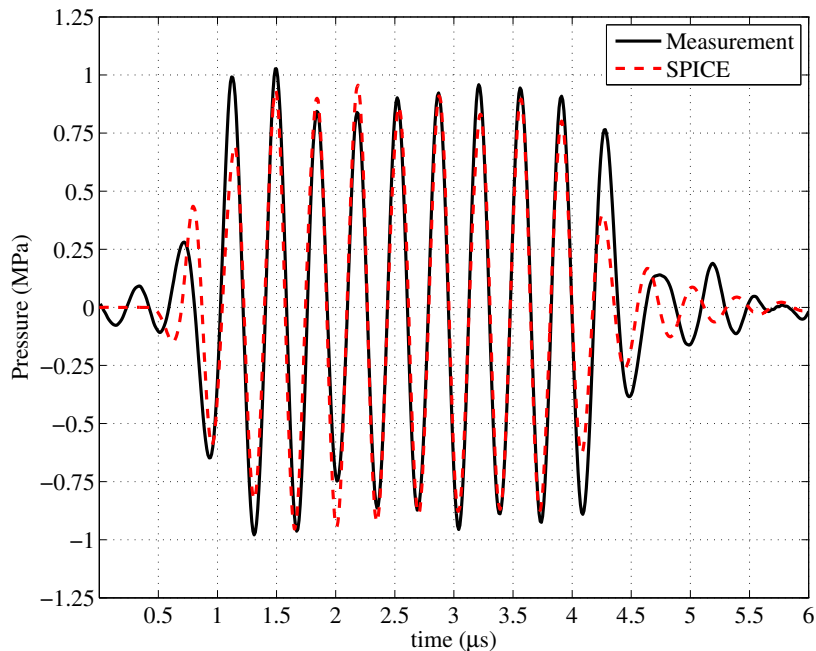


Figure 7.6: 5 cycle 125V_{peak} cosine burst at 1.44 MHz is applied to the CMUT element. After the measurement is corrected for diffraction, and attenuation losses; the result is multiplied by $Z_r(w)/R_r(w)$ in frequency domain and its inverse fourier transform is compared to the pressure obtained from SPICE model.

Chapter 8

Conclusion & Future Directions

The proposed model can be used to accurately simulate the behavior of a CMUT for the uncollapsed region, which is suitable for low harmonic high power applications. Using the proposed model, the CMUT parameters can be optimized in a faster way when compared to FEM. By creating the model in a SPICE simulator, the simulation of a fluid loaded array can be done within seconds. Furthermore, the circuit can be used as a CMUT front-end IC test bench to optimize the ICs performance before fabrication.

Higher radiation impedance improves the transducers performance. For the given voltage and for the given total transducer area, the cMUT cell radius should be chosen to maximize the radiation resistance at the operating frequency to get higher power.

Driving CMUTs at half of their resonance frequency eliminates the problems caused by the charge trapping the insulation dielectric. The membrane moves symmetrically in both directions around a stable deflection point. At the optimum operation, the center of the membrane swings in a distance of more than the gap height. Using anodic bonding it is possible to fabricate CMUTs with thick membranes and low gap heights at low temperature. The process provides high control over the CMUT parameters.

The measurements show that CMUT technology is a strong candidate for HIFU operation. The observed surface pressure is a record level for continuous wave operation. The second harmonic level is around -30 dB and can be reduced by operating at lower peak voltages. The available voltage has an important impact over the output pressure. When a higher input voltage level is provided, with the proposed methodology for the design, the volume displacement of the membrane increases for the optimum design because the resulting gap height increases.

The control over layer thicknesses is important in fabrication. In a well equipped clean room facility, a more precise fabrication would be done in order to realize the optimum design.

The measured pressures are on the surface of the CMUT element. Focusing can be done with a phased array that consists of optimized CMUT elements by using the methodology described in this thesis. An overall system design with driving electronics would be the future goal for a targeted HIFU operation.

Chapter 9

Appendix

9.1 FEM Model

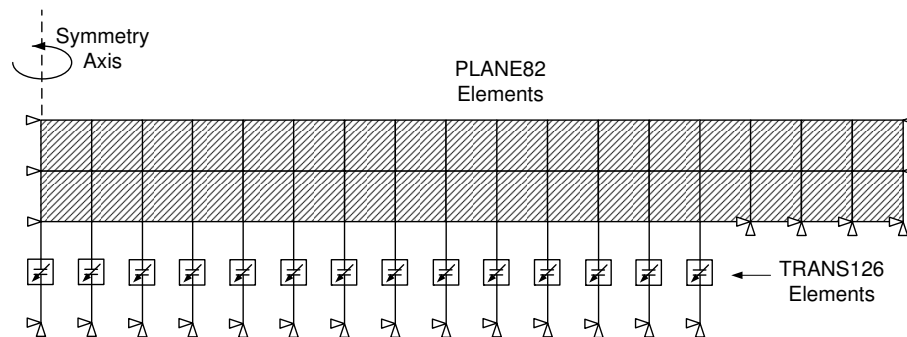


Figure 9.1: Representative finite element model of the transducer created in ANSYS. Membrane is modeled with PLANE82 elements. TRANS126 elements are generated using EMTGEN command.

The FEM model is created using ANSYS (v13.0) Multiphysics Environment. An 2-D axissymmetric model is created to simulate single CMUT cell behavior 9.1. Predefined elements are used to generate the model. 2-D 8-Node Structural Solid PLANE82 elements are used to model the membrane. The fluid medium is modeled using FLUID29 elements. Absorption is activated by using FLUID129 elements on the outer surface of FLUID29 elements to extend the fluid domain. The fluid structure interaction is activated over the membrane surface. Electromechanical trans-

ducer elements, TRANS126, were generated under the bottom surface nodes of the membrane using "EMTGEN command. The command requires a gap value, GAP, to generate ground plane nodes under the selected nodes and creates TRANS126 elements in between. The macro also performs a point-wise capacitance calculation and provides the necessary inputs for each TRANS126 element. The GAPMIN parameter entered in the command defines where the contact occurs.

The TRANS126 element is lack of modeling the insulating layer, thus the required input parameters (GAP and $GAPMIN$) for the TRANS126 element are modified to perform a realistic capacitance calculation considering the insulating layer thickness of the fabricated CMUTs. The modified parameters are calculated as follow;

$$GAP = t_g + \frac{t_i}{\epsilon} \quad (9.1)$$

$$GAPMIN = \frac{t_i}{\epsilon} \quad (9.2)$$

The performance of the model with the modified parameters is verified by contact elements. CONTA172 / TARGE169 element pairs are replaced between the membrane and the substrate nodes. The static deflection profile of a CMUT in collapse state is plotted for both cases in Fig. 9.2. The simulations with contact elements are more realistic as the pair elements include the sliding effect of the membrane over the substrate when it collapses. However, the simulations with TRANS126 elements takes considerably less time.

The model including the fluid medium is shown in Fig. 9.3.

The 2-D FEM model described here is first used for the static analysis. The modal analysis are done to get the resonant frequency of CMUT in air. The resonant frequency in fluid medium is found by doing harmonic analysis. The transient analysis are done in the fluid medium to get the peak displacement of the membrane

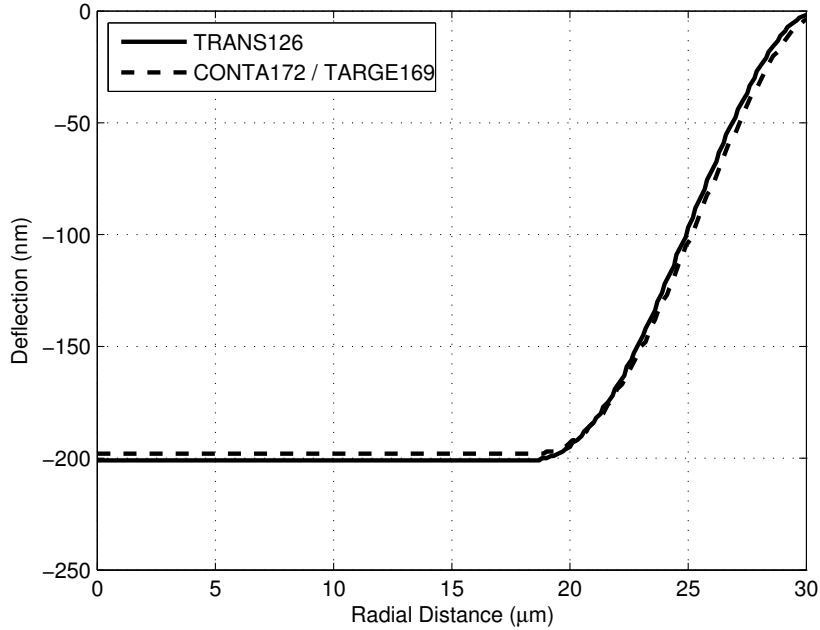


Figure 9.2: Comparison of the deflection profile of a CMUT in collapse state simulated using for TRANS126 and CONTA172/TARGE169 contact elements. CMUT parameters: $a = 30 \mu\text{m}$, $t_m = 1.4 \mu\text{m}$, $t_g = 200 \text{ nm}$, $t_i = 0.4 \mu\text{m}$

under a CW signal. In the transient analysis, the transient effects are turned off in the first step to observe a stable membrane under the DC bias. And then, transient effects are turned on and the analysis is performed.

The 2-D axisymmetric model can also simulate the behavior of an infinite CMUT array. In that case, rather using a circular absorbing boundary a rigid fluid column is created over the membrane. The rigid fluid column creates a mirror effect and reflects pressure waves on its walls, so that the model sees the same field from the walls of the fluid column and assumes that the membrane is covered with CMUT cells 9.4.

To simulate the behavior of a CMUT array with finite number of cells, a 3D model is required. 3-D models require a volumetric mesh which increases the number of nodes dramatically in the model. Thus, the simulation time that is required to simulate an array of 7 CMUT cell with fluid loading becomes unfeasible. To decrease

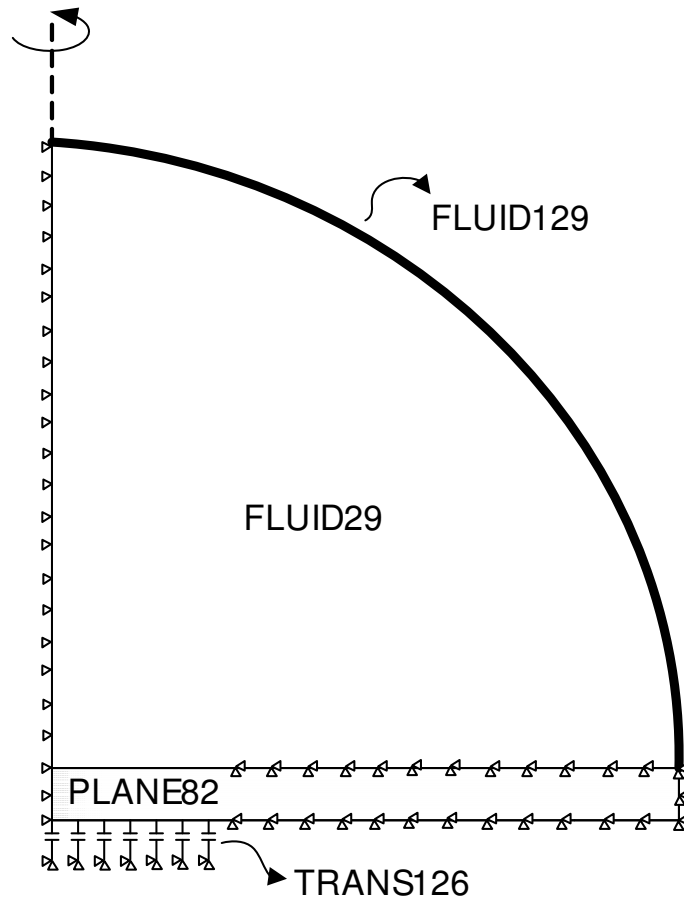


Figure 9.3: Representative finite element model including the fluid medium which is extended using FLUID129 absorbing elements.

the simulation time, we get benefit from the inherent symmetry of the model, the analysis's are performed on a quarter symmetry model as shown in Fig. 9.5. In 3D model, the membrane is modeled using SOLID186 elements and the fluid medium is modeled using FLUID220. The fluid element provides a perfectly matched layer (PML) option to absorb the outgoing sound waves. Hence, the outer fluid elements are modified to act as a PML layer.

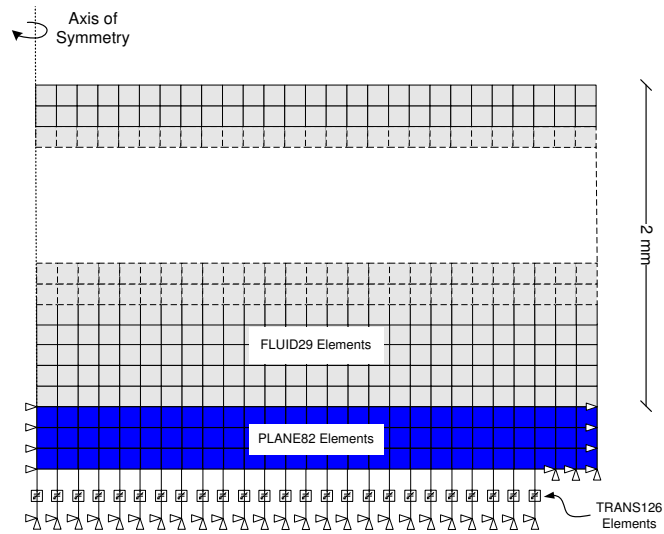


Figure 9.4: The FEM model of a CMUT element with infinite cells.

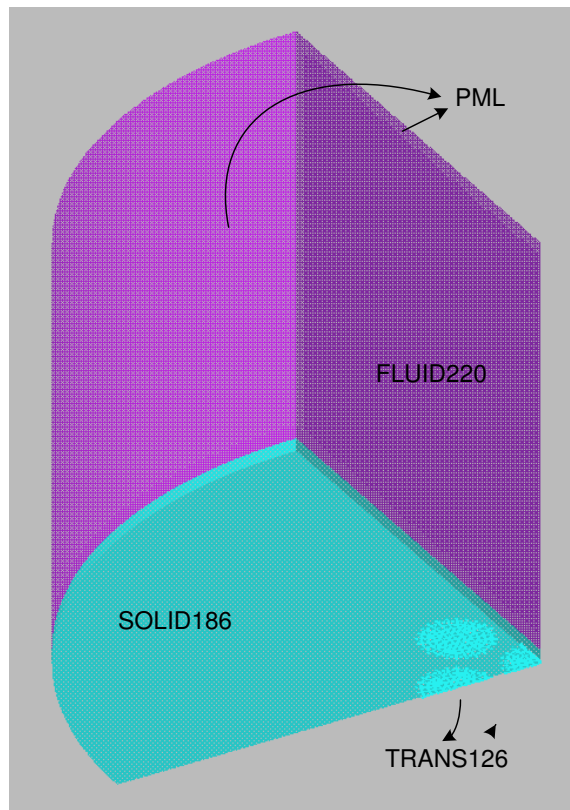


Figure 9.5: 3D FEM model of a CMUT element with 7 cells. A quarter model of the array and the fluid medium is used for the simulations.

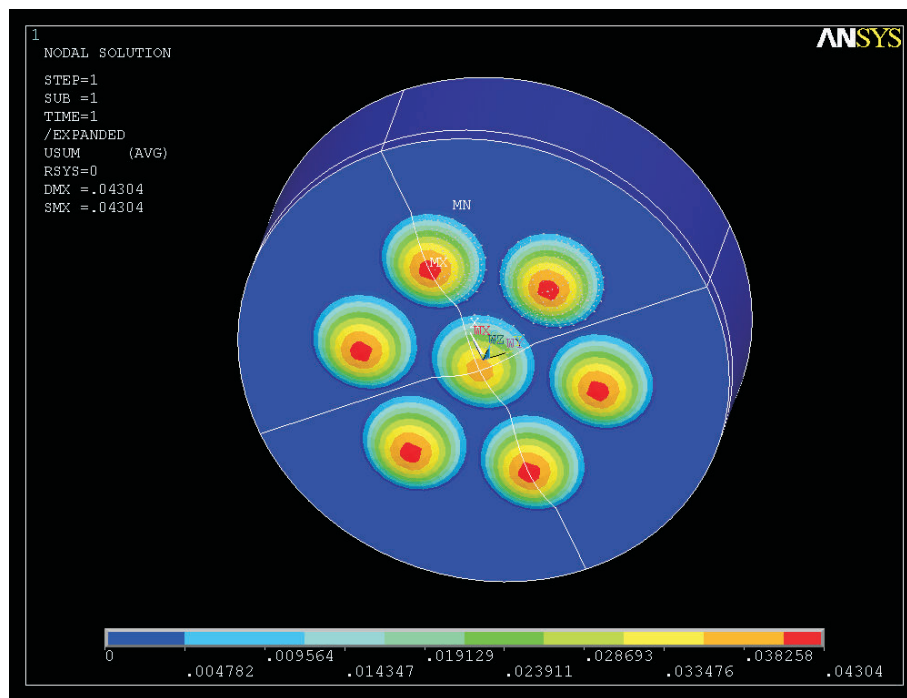


Figure 9.6: Expanded view of the 3D quarter model of a CMUT element with 7 cells.

Bibliography

- [1] M. I. Haller and B. T. Khuri-Yakub, “A surface micromachined electrostatic ultrasonic air transducer,” *IEEE Trans. Ultrason., Ferroelect., Freq. Contr.*, vol. 43, pp. 1–6, 1996.
- [2] X. Jin, I. Ladabaum, and B. T. Khuri-Yakub, “The microfabrication of capacitive micromachined ultrasonic transducers,” *J. Microelectromech. Syst.*, vol. 7, pp. 295–302, 1998.
- [3] I. Ladabaum, X. Jin, H. T. Soh, A. Atalar, and B. T. Khuri-Yakub, “Surface micromachined capacitive ultrasonic transducers,” *IEEE Trans. Ultrason., Ferroelect., Freq. Contr.*, vol. 45, pp. 678–690, 1998.
- [4] B. Bayram, Ö. Oralkan, A. S. Ergun, E. Hægström, G. G. Yaralioglu, and B. T. Khuri-Yakub, “Capacitive micromachined ultrasonic transducer design for high power transmission,” *IEEE Trans. Ultrason., Ferroelect., Freq. Contr.*, vol. 52, pp. 326–339, 2005.
- [5] Ö. Oralkan, B. Bayram, G. G. Yaralioglu, A. S. Ergun, M. Kupnik, D. T. Yeh, I. O. Wygant, and B. T. Khuri-Yakub, “Experimental characterization of collapse-mode CMUT operation,” *IEEE Trans. Ultrason., Ferroelect., Freq. Contr.*, vol. 53, pp. 1513–1523, 2006.
- [6] Ö. Oralkan, A. S. Ergun, J. A. Jhonson, M. Karaman, U. Demirci, K. Kaviani, T. H. Lee, and B. T. Khuri-Yakub, “Capacitive micromachined ultrasonic transducers: Next-generation arrays for acoustic imaging?” *IEEE Trans. Ultrason., Ferroelect., Freq. Contr.*, vol. 49, pp. 1596–1610, 2002.

- [7] D. Memmi, V. Foglietti, E. Cianci, G. Caliano, and M. Pappalardo, “Fabrication of capacitive micromechanical ultrasonic transducers by low-temperature process,” *Sens. and Actuat. A*, vol. 99, pp. 85–91, 2002.
- [8] F. L. Degertekin, R. O. Guldiken, and M. Karaman, “Annular-ring cmut arrays for forward-looking ivus: transducer characterization and imaging,” *IEEE Trans. Ultrason., Ferroelect., Freq. Contr.*, vol. 53, pp. 474–482, 2006.
- [9] K. K. Park, H. Lee, M. Kupnik, and B. Khuri-Yakub, “Fabrication of capacitive micromachined ultrasonic transducers via local oxidation and direct wafer bonding,” *Microelectromechanical Systems, Journal of*, vol. 20, no. 1, pp. 95–103, feb. 2011.
- [10] A. S. Ergun, Y. Huang, X. Zhuang, O. Oralkan, G. G. Yaralioglu, and B. T. Khuri-Yakub, “Capacitive micromachined ultrasonic transducers: fabrication technology,” *IEEE Trans. Ultrason., Ferroelect., Freq. Contr.*, vol. 52, pp. 2242–2258, 2005.
- [11] S. Zhang, R. Xia, L. Lebrun, D. Anderson, and T. R. Shrout, “Piezoelectric materials for high power, high temperature applications,” in *Matter. Lett.*, 2005, pp. 3471–3475.
- [12] S. Yarlagadda, M. H. Chan, H. Lee, G. A. Lesieutre, D. W. Jensen, and R. S. Messer, “Low temperature thermal conductivity, heat capacity, and heat generation of pzt,” *Journal of Intelligent Material Systems and Structures*, vol. 6, no. 6, pp. 757–764, November 1995.
- [13] J. F. Schenck, “The role of magnetic susceptibility in magnetic resonance imaging: Mri magnetic compatibility of the first and second kinds,” *Med. Phys.*, vol. 23, pp. 815–850, 1996.
- [14] S. H. Wong, M. Kupnik, R. D. Watkins, K. Butts-Pauly, and B. T. Khuri-Yakub, “Capacitive micromachined ultrasonic transducers for therapeutic ultrasound applications,” *IEEE Trans. Ultrason., Ferroelect., Freq. Contr.*, vol. 57, pp. 114–123, 2010.

- [15] S. H. Wong, R. D. Watkins, M. Kupnik, K. B. Pauly, and B. T. Khuri-Yakub, “Feasibility of MR-temperature mapping of ultrasonic heating from a CMUT,” *IEEE Trans. Ultrason., Ferroelect., Freq. Contr.*, vol. 55, pp. 811–818, 2008.
- [16] S. Olcum, F. Y. Yamaner, A. Bozkurt, H. Köymen, and A. Atalar, “Deep collapse operation of capacitive micromachined ultrasonic transducers,” *Submitted.*, 2010.
- [17] H. K. Oguz, S. Olcum, M. N. Senlik, V. Tas, A. Atalar, and H. Köymen, “Nonlinear modeling of an immersed transmitting capacitive micromachined ultrasonic transducer for harmonic balance analysis,” *IEEE Trans. Ultrason., Ferroelect., Freq. Contr.*, vol. 57, pp. 438–447, 2010.
- [18] J. E. Kennedy, G. R. ter Haar, and D. Cranston, “High intensity focused ultrasound: surgery of the future?” *British Journal of Radiology*, no. 76, pp. 590–599, 2003.
- [19] W. J. Fry, “Precision high intensity focusing ultrasonic machines for surgery,” *Am. J. Phys. Med.*, vol. 37, pp. 152–156, 1958.
- [20] J. E. Zimmer, K. Hynynen, D. S. He, and F. Marcus, “The feasibility of using ultrasound for cardiac ablation,” vol. 42, no. 9, pp. 891–897, 1995.
- [21] M. D. Brentnall, R. W. Martin, S. Vaezy, P. Kaczkowski, F. Forster, and L. Crum, “A new high intensity focused ultrasound applicator for surgical applications,” vol. 48, no. 1, pp. 53–63, 2001.
- [22] H. Wan, P. VanBaren, E. S. Ebbini, and C. Cain, “Ultrasound surgery: comparison of strategies using phased array systems,” vol. 43, no. 6, pp. 1085–1098, Nov 1996.
- [23] I. H. Rivens, R. L. Clark, and G. R. Haar, “Design of focused ultrasound surgery transducers,” vol. 43, no. 6, pp. 1023–1031, Nov. 1996.
- [24] G. R. Haar, R. L. Clarke, M. G. Vaughan, and C. R. Hill, “Trackless surgery using focused ultrasound: technique and case report,” *Minimally Invasive Therapy*, vol. 1, pp. 13–19, 1991.

- [25] F. Wu, W. Z. Chen, J. Bai, J. Z. Zou, Z. L. Wang, H. Zhu, and et al., “Pathological changes in human malignant carcinoma treated with high intensity focused ultrasound,” *Ultrason. Med. Biol.*, vol. 27, p. 10991106, 2001.
- [26] K. Hynynen, O. Pomeroy, D. N. Smith, P. E. Huber, N. J. McDannold, J. Kettenbach, and et. al., “Mr imaging-guided focused ultrasound surgery of fibroadenomas in the breast; a feasibility study,” *Radiology*, vol. 219, p. 176185, 2001.
- [27] G. S. Chen, H. Chang, R. Liu, and K. K. Shung, “Development of 1.5d cylindrical hifu phased array,” in *Proc. IEEE Ultrason. Symp.*, vol. 4, pp. 792–794, 2008.
- [28] R. Illing and M. Emberton, “Sonablate-500: transrectal high-intensity focused ultrasound for the treatment of prostate cancer,” *Expert Rev. Med. Devices*, vol. 3, no. 6, p. 717729, 2006.
- [29] C. Chaussy and S. Thuroff, “High intensity focused ultrasound in prostate cancer: Results after 3 years,” *Molec. Urol.*, vol. 4, pp. 179–182, 2000.
- [30] B. Bayram, E. Hæggström, G. G. Yaralioglu, and B. T. Khuri-Yakub, “A new regime for operating capacitive micromachined ultrasonic transducers,” *IEEE Trans. Ultrason., Ferroelect., Freq. Contr.*, vol. 50, pp. 1184–1190, 2003.
- [31] Y. Huang, X. Zhuang, E. Hggstrom, A. Ergun, C.-H. Cheng, and B. Khuri-Yakub, “Capacitive micromachined ultrasonic transducers with piston-shaped membranes: fabrication and experimental characterization,” *Ultrasonics, Ferroelectrics and Frequency Control, IEEE Transactions on*, vol. 56, no. 1, pp. 136–145, january 2009.
- [32] M. Senlik, S. Olcum, and A. Atalar, “Improved performance of cmut with nonuniform membranes,” in *Ultrasonics Symposium, 2005 IEEE*, vol. 1, sept. 2005, pp. 597 – 600.
- [33] E. S. Hung and S. D. Senturia, “Extending the travel range of analog-tuned electrostatic actuators,” *Journal of MEMs*, vol. 8, pp. 497–505, 1999.

- [34] J. McLean, R. O. Guldiken, and F. L. Degertekin, “CMUTs with dual electrode structure for improved transmit and receive performance,” in *Proc. IEEE Ultrason. Symp.*, 2004, pp. 501–504.
- [35] R. O. Guldiken, J. Zahorian, F. Y. Yamaner, and F. L. Degertekin, “Dual-electrode CMUT with non-uniform membranes for high electromechanical coupling coefficient and high bandwidth operation,” *IEEE Trans. Ultrason., Ferroelect., Freq. Contr.*, vol. 56, pp. 1270–1276, 2009.
- [36] A. Bozkurt, I. Ladabaum, A. Atalar, and B. T. Khuri-Yakub, “Theory and analysis of electrode size optimization for capacitive microfabricated ultrasonic transducers,” *IEEE Trans. Ultrason., Ferroelect., Freq. Contr.*, vol. 46, pp. 1364–1374, 1999.
- [37] A. Lohfink and P. C. Eccardt, “Linear and nonlinear equivalent circuit modeling of CMUTs,” *IEEE Trans. Ultrason., Ferroelect., Freq. Contr.*, vol. 52, pp. 2163–2172, 2005.
- [38] H. Kagan Oguz, S. Olcum, M. Senlik, A. Atalar, and H. Köymen, “A novel equivalent circuit model for cmuts,” in *Ultrasonics Symposium (IUS), 2009 IEEE International*, sept. 2009, pp. 2193 –2196.
- [39] H. Köymen, M. N. Senlik, A. Atalar, and S. Olcum, “Parametric linear modeling of circular CMUT membranes in vacuum,” *IEEE Trans. Ultrason., Ferroelect., Freq. Contr.*, vol. 54, pp. 1229–1239, 2007.
- [40] I. O. Wygant, M. Kupnik, and B. T. Khuri-Yakub, “Analytically calculating membrane displacement and the equivalent circuit model of a circular cmut cell.” in *Proc. IEEE Ultrason. Symp.*, 2008, pp. 2111–2114.
- [41] M. N. Senlik, S. Olcum, H. Köymen, and A. Atalar, “Radiation impedance of an array of circular capacitive micromachined ultrasonic transducers,” *IEEE Trans. Ultrason., Ferroelect., Freq. Contr.*, vol. 57, pp. 969–976, 2010.

- [42] A. Bozkurt and M. Karaman, “A lumped circuit model for the radiation impedance of a 2d cmut array element,” in *Ultrasonics Symposium, 2005 IEEE*, vol. 4, sept. 2005, pp. 1929 – 1932.
- [43] S. Machida, S. Migitaka, H. Tanaka, K. Hashiba, H. Enomoto, Y. Tadaki, and T. Kobayashi, “Analysis of the charging problem in capacitive micro-machined ultrasonic transducers,” in *Proc. IEEE Ultrason. Symp.*, 2008, pp. 383–385.
- [44] K. Midtbo and A. Ronnekleiv, “Analysis of charge effects in high frequency CMUTs,” in *Proc. IEEE Ultrason. Symp.*, 2008, pp. 379–382.
- [45] J. Knight, J. McLean, and F. L. Degertekin, “Low temperature fabrication of immersion capacitive micromachined ultrasonic transducers on silicon and dielectric substrates,” *IEEE Trans. Ultrason., Ferroelect., Freq. Contr.*, vol. 51, pp. 1324–1333, 2004.
- [46] B. Belgacem, D. Alquier, P. Muralt, J. Baborowski, S. Lucas, and R. Jerisian, “Optimization of the fabrication of sealed capacitive transducers using surface micromachining,” *J. Micromech. Microeng.*, vol. 14, pp. 299–304, 2004.
- [47] E. Cianci, L. Visigalli, V. Foglietti, G. Caliano, and M. Pappalardo, “Improvements towards a reliable fabrication process for cMUT,” *Microelec. Eng.*, vol. 67–68, pp. 602–608, 2003.
- [48] L. L. Liu, O. M. Mukdadi, C. F. Herrmann, R. A. Saravanan, J. R. Hertzberg, S. M. George, V. M. Bright, and R. Shandas, “A novel method for fabricating capacitive micromachined ultrasonic transducers with ultra-thin membranes,” in *Proc. IEEE Ultrason. Symp.*, 2004, pp. 497–500.
- [49] Y. Huang, A. S. Ergun, E. Hæggröm, M. H. Badi, and B. T. Khuri-Yakub, “Fabricating capacitive micromachined ultrasonic transducers with wafer-bonding technology,” *J. Microelectromech. Syst.*, vol. 12, pp. 128–137, 2003.
- [50] S. H. Wong, M. Kupnik, X. Zhuang, D.-S. Lin, K. Butts-Pauly, and B. T. Khuri-Yakub, “Evaluation of wafer bonded CMUTs with rectangular membranes fea-

- turing high fill factor,” *IEEE Trans. Ultrason., Ferroelect., Freq. Contr.*, vol. 55, pp. 2053–2065, 2008.
- [51] R. Chanamai and D. J. McClements, “Ultrasonic attenuation of edible oils,” *J. Amer. Oil. Chem.*, vol. 75, pp. 1447–1448, 1998.